

UC Riverside

UC Riverside Electronic Theses and Dissertations

Title

MEMS-based Massively-parallelized Mechanoporation Instrumentation for Ultrahigh Throughput Cellular Manipulation

Permalink

<https://escholarship.org/uc/item/2fj0171t>

Author

Zhang, Yanyan

Publication Date

2012

Peer reviewed|Thesis/dissertation

UNIVERSITY OF CALIFORNIA
RIVERSIDE

MEMS-based Massively-parallelized Mechanoporation Instrumentation for Ultrahigh
Throughput Cellular Manipulation

A Dissertation submitted in partial satisfaction
of the requirements for the degree of

Doctor of Philosophy

in

Mechanical Engineering

by

Yanyan Zhang

December 2012

Dissertation Committee:

Dr. Masaru P. Rao, Chairperson

Dr. Hideaki Tsutsui

Dr. Guillermo Aguilar

Copyright by
Yanyan Zhang
2012

The Dissertation of Yanyan Zhang is approved:

Committee Chairperson

University of California, Riverside

ACKNOWLEDGEMENTS

First, I would like to thank my advisor Professor Masaru Rao for providing me with valuable opportunities and excellent guidance during my study at University of California - Riverside in the past four years. Professor Rao contributes a lot to my academic development with his brilliant ideas and rich experiences. He is always there supporting me with my class materials, research studies and personal life. I will remember all the time that Professor Rao's professional views and kind suggestions helped me improved greatly not only in academic field but also in personal development.

I would like to thank Professor Chris Ballas for collaborating with us and helping us develop our cell test models and solve related problems. I want to thank Professor Hideaki Tsutsui for serving as my defense committee and for collaborating with us, as well as his helpful advices and support for our cell studies. I also would like to thank Professor Guillermo Aguilar for serving as my defense committee and his suggestions as Graduate Advisor.

Thanks are also given to my colleagues in the Laboratory of Biomedical Microdevices for their kind help and hard working in laboratory experiments as well as friendly supports: graduated students Mr. Daniel Nampe, Mr. Harish Dixit, Ms. Shannon Gott, Mr. Omid Khandan, Mr. Justin Mueller, and undergraduate student Ms. Camila Villanueva. Besides, I would like to thank the staffs in the Center for Nanoscale Science & Engineering in University of California – Riverside, in the Integrated Nanosystems Research Facility in University of California – Irvine, and in the Nanotech – the UCSB Nanofabrication Facility in University of California – Santa Babara: Mr. Dong Yan, Mr.

Dexter Humphrey, Mr. Vu Phan, Mr. Jake Hes, and Mr. Brian Thibeault, for their professional suggestions and kind helps. Also thank all my friends in University of California - Riverside for their friendships and support whenever I got difficulties in my research, study and life.

Special thanks go to my parents for their endless love and encouragement, and my granduncle, grandaunt and uncle, who are my family in the USA and give me warm support all the time.

My research was supported by the project under Grant# 8 R21GM0103973 from NIH/NIGMS.

ABSTRACT OF THE DISSERTATION

MEMS-based Massively-parallelized Mechanoporation Instrumentation for Ultrahigh Throughput Cellular Manipulation

by

Yanyan Zhang

Doctor of Philosophy, Graduate Program in Mechanical Engineering

University of California, Riverside, December 2012

Dr. Masaru P. Rao, Chairperson

Many applications in cell biology, genetic engineering, cell-based therapeutics, and drug discovery require precise and safe methods for introducing membrane-impermeable molecules into cells. This can be implemented satisfactorily by microinjection. However, disadvantages of traditional manual microinjection include high degree of operator skill, low throughput and labor-intensiveness. Many studies have focused on developing automated and high-throughput systems for microinjection to address these limitations. However, none have provided sufficient throughput for applications such as *ex vivo* cell therapy, where manipulation of many millions of cells is required. Herein, we propose an ultrahigh throughput (UHT) mechanoporation concept that seeks to address these limitations. The mechanoporation device is a massively-parallelized MEMS-based platform for passively delivering molecules into living cells via mechanical cell membrane penetration. Studies focusing on device design, fabrication and validation at the proof-of-concept level are presented in this dissertation.

Detailed system concept and design is introduced, which integrates functions of cell transfer, capture, penetration and release into a single piece of instrumentation using

a microfluidic approach. System operating parameters are analytically analyzed and numerically simulated. Results from these studies agree with previous studies by others in related applications, and suggest reasonable operation feasibility without detrimental effect on cells. Those estimated operation parameters also provide basis to develop test models in practical cell studies. The device fabrication utilized conventional silicon MEMS technologies, and we successfully produced millimeter-scale device chips containing an array of ten thousand hemispherical capture wells with monolithically integrated solid penetrators. A flow circuit system involving a syringe pump, pressure transducer, and fixture set supporting the device chip was developed, and preliminary functional testing was carried out. Device validation tests using K562 cells obtained about 15% average penetration efficiency of live cells after manipulation. Subsequent testing with fluorescent beads and Mouse Embryonic Fibroblast (MEF) cells identified several key issues responsible for the lower-than-expected efficiency, thus suggesting that improved performance may be possible with further system and operation optimization.

The UHT mechanoporation device developed in this effort shows promise for providing an efficient and safe method for introducing membrane impermeable molecules into cells with ultrahigh throughput. Moreover, these studies also represent key steps towards our long-term goal of developing instrumentation capable of UHT cellular manipulation via active microinjection. This new instrumentation will have broad potential for advancing understanding of fundamental cellular processes, as well as facilitating clinical translation of cell-based therapies.

CONTENTS

1. Introduction.....	1
1.1 Cellular molecular delivery manipulation	1
1.1.1 Cellular molecular delivery applications.....	1
1.1.2 Biological delivery method	1
1.1.3 Chemical delivery method	1
1.1.4 Physical delivery method	2
1.2 Cellular molecular delivery by microinjection	3
1.2.1 Traditional manual microinjection	3
1.2.2 Semi-automated microinjection systems.....	4
1.2.3 Passive automated microinjection	6
1.2.4 Microfluidic manner based automated cell injection system	7
1.3 Dissertation outline.....	8
2. Instrumentation Design.....	10
2.1 Instrumentation concept	10
2.2 Device design	12
2.3 Operation parameter estimation.....	13
2.3.1 Cell membrane penetration force estimation	13
2.3.2 Cell speed estimation	19
2.3.3 Pressure drop and cell solution speed numerical simulation.....	21
2.3.4 Conclusion.....	26
3. Device Fabrication	28

4. Device characterization.....	45
4.1 Preliminary functional verification.....	45
4.1.1 Fixture set construction.....	45
4.1.2 Flow circuit development.....	46
4.1.3 Leaking elimination.....	46
4.1.4 Pressure validation	47
4.2 Cell tests	47
4.2.1 K562Cell tests	49
4.2.2 Fluorescent beads tests	51
4.2.3 MEF cell tests.....	55
5. Future Directions	58
5.1 UHT active microinjection device chip fabrication	60
5.2 Affiliated system development.....	62
6. Conclusion	63
References.....	65

LIST OF FIGURES

Figure 1.1 Manual operation of gene delivery microinjection into living cells.....	4
Figure 1.2 Anchoring cells by capillary force [28].....	5
Figure 1.3 Dent structure for cell capturing by aspiration pressure [26].....	5
Figure 1.4 A schematic drawing of the proposed concept for a high-throughput microinjection system using both microneedle arrays and cell arrays [28].....	7
Figure 1.5 a) Schematic of carbon nanosyringe arrays with cell seeding; b) SEM images of carbon nanosyringe arrays with exposed heights of 80 nm and 120 nm [34].....	7
Figure 1.6 Schematic representation of the microfluidic manner based automated single cell microinjection system [25].....	8
Figure 2.1 Schematic of a proposed UHT active microinjection instrumentation concept. Arrows denote flow direction and magnitude.	11
Figure 2.2 Schematic of the proposed UHT mechanoporation instrumentation concept. Arrows denote flow direction and magnitude.	11
Figure 2.3 Schematics of single UHT mechanoporation instrument Capture Site monolithically integrated with solid penetrator, and four elliptical aspiration vias at the bottom, which are connecting with aspiration port.....	12

Figure 2.4 Schematics of penetration force in linear relationship with elastic modulus in the condition of K562 cell membrane penetration force calculation.	15
Figure 2.5 Schematics of elliptical aspiration via's cross section in coordinate system to calculate flow velocity flowing through the via in z direction.....	17
Figure 2.6 Schematics of penetration force in linear relationship with indenter's tip size in the condition of MEF cell membrane penetration force calculation.	18
Figure 2.7 Numerical simulation results of (a) velocity magnitude field (b) velocity vector field and (c) pressure field adjacent to Solid Penetrator and in vias, under steady state condition during K562 cell transportation before cell being captured on Solid Penetrator.	22
Figure 2.8 Numerical simulation results of (a) velocity magnitude field (b) velocity vector field and (c) pressure field adjacent to Solid Penetrator and in vias, under steady state condition at the moment that K562 cell is captured on Solid Penetrator.....	23
Figure 2.9 Numerical simulation results of (a) velocity magnitude field (b) velocity vector field and (c) pressure field adjacent to Solid Penetrator and in vias, under steady state condition during MEF cell transportation before cell being captured.	24

Figure 2.10 Numerical simulation results of (a) velocity magnitude field (b) velocity vector field and (c) pressure field adjacent to Solid Penetrator and in vias under steady state condition after MEF cell being captured on solid penetrator.	25
Figure 3.1 Device microfabrication process flow. Only one Capture Site is shown for the sake of clarity.	29
Figure 3.2 SEM images of elliptical via patterns. (a) Four elliptical vias to create single capture well and Solid Penetrator later; (b) Lower magnification view of a portion of the elliptical vias array.	34
Figure 3.3 Optical microscope image of a portion of the 100 by 100 capture site array after isotropic etching.	35
Figure 3.4 SEM images of capture wells and Solid Penetrators after isotropic etching and via anisotropic etching. (a) Single capture well monolithically integrated with Solid Penetrator; (b) Lower magnification of a portion of the 100 x 100 capture site array.	36
Figure 3.5 SEM image of Focused Ion Beam Milled single via's cross section.	36
Figure 3.6 SEM images of capture wells and solid penetrators after Cl ₂ etching. (a) Single capture well monolithically integrated with Solid Penetrator; (b) Higher magnification view and measurement of the single Solid Penetrator top; (c) Higher magnification view and measurement of the single Solid Penetrator passivation wildest part;	

(d) Lower magnification of a portion of the 100 x 100 capture site array.....	39
-------------------------------------------------------------------------------	----

Figure 3.7 SEM images of capture wells and Solid Penetrators after Chlorine passivation removal dry etching. (a) Single capture well monolithically integrated with Solid Penetrator; (b) Higher magnification view of the single Solid Penetrator, with about 342nm by 928 nm sharp top; (c) Lower magnification of a portion of the 100 x 100 capture site array.	41
--------------------------------------------------------------------------------------------------------------------------------------------------------------------------------------------------------------------------------------------------------------------------------------------------------------------------------------------------------------------------	----

Figure 3.8 SEM images of handle layer of device chip. (a) Four vias within single capture site connecting with big Aspiration port; (b) Lower magnification view of a portion of the 100 x 100 vias array; (c) View of aspiration big ports on handle layer of substrate.....	44
-------------------------------------------------------------------------------------------------------------------------------------------------------------------------------------------------------------------------------------------------------------------------------	----

Figure 4.1 Schematic of the fixture set. (Left): bottom part of the fixture set, holding device chip in the middle reservoir. (Right): top part of the fixture set.....	45
-------------------------------------------------------------------------------------------------------------------------------------------------------------------------	----

Figure 4.2 (a) Comparison between measured infusion pressure readings from several tests and analytical calculation results. (b) Comparison between measured withdraw pressure readings from several tests and analytical calculation results. Plotted measurements are averaged values at each flow rate for 3 separate tests. Error bars represent standard deviation.....	48
------------------------------------------------------------------------------------------------------------------------------------------------------------------------------------------------------------------------------------------------------------------------------------------------------------------------------------------------------------------------------	----

Figure 4.3 Flow cytometry results for UHT mechanoporation device: (Left) Scatter plots (cell size/granularity) showing non-porated cells occupying larger population in center of plots and porated cells occupying population near side scatter axis; (Right) Histograms of cells pooled from 15 operation cycles showing overall poration efficiency of ~15% (percent dye positive cells indicated on each plot). 50

Figure 4.4 Images of UHT mechanoporation device chip test setting: (a) Entire setting including syringe pump, pressure meter, fixture set with device chip, and microscope; (b) Fixture set with device chip sitting under microscope. 52

Figure 4.5 Fluorescence images of: (a) bubbles being trapped underneath capture well arrays and (b) bubbles being completely eliminated from capture well arrays after rigorous flushing..... 53

Figure 4.6 Fluorescence images of polystyrene beads' population on device chip with different flow rate and time: (a) bead's population (about 9.6%) with flow rate 10 $\mu\text{L}/\text{min}$ for 2 min; (b) bead's population (about 20%) with flow rate 20 $\mu\text{L}/\text{min}$ for 2 min; (c) bead's population (about 75.2%) with flow rate 40 $\mu\text{L}/\text{min}$ for 1 min; (d) Higher magnification of lined up beads with flow rate 40 $\mu\text{L}/\text{min}$ 54

Figure 4.7 Fluorescence images of MEF cells population at a fixed position in the capture site array during an operation cycle: (a) Cell capturing started at flow rate $10 \mu\text{L}/\text{min}$; (b) Washing away excess uncaptured cells with pipette at 60 sec while capturing aspiration pressure is still provided; (c) Stop cell capturing at 110 sec and change pump flow rate to $70 \mu\text{L}/\text{min}$; Cell puncture started at 125 sec at flow rate $70 \mu\text{L}/\text{min}$; (d) Stop cell puncturing at 165 sec.	55
Figure 4.8 Pressure change plot from pressure transducer recording during the MEF cell study and a control study.	57
Figure 5.1 Schematic of a portion of the UHT active microinjection device.	58
Figure 5.2 Schematics of the UHT active microinjection device and affiliated parts.	59
Figure 5.3 Abridged microfabrication process flow for UHT active microinjection device. Dotted line indicates the bonded interface. Only one unit cell site is shown for the sake of clarity.	61

LIST OF TABLES

Table 2.1 List of cell types, cell membrane mechanical properties, cell membrane penetration forces and injector tip sizes from other research studies.	16
Table 2.2 Constants in equation (2.2) for cell speeds calculation.	20
Table 4.1 Penetration efficiency of K562 cells from manual hemacytometric counting.	49

1. Introduction

1.1 Cellular molecular delivery manipulation

1.1.1 Cellular molecular delivery applications

The delivery of membrane-impermeable molecules into living cells is needed for a broad variety of applications, such as molecular and cell biology [1], genetic engineering [2-5], drug development [6], and cell-based therapy [4, 7, 8]. Specifically, cell based therapy has been applied for fatal infections like AIDs [9], cancers [10], tumors and genetic diseases. There are several technologies of cellular molecule delivery currently in use, including, biological, chemical and physical approaches.

1.1.2 Biological delivery method

Biological methods by using virus vector or carrier peptide has many undesired side effects, e.g. safety concerns such as viral toxicity, host immune rejection and infection, etc [11]. In the meanwhile, the method needs time-consuming preparation, and it is expensive as well as impossible to determine how many molecules are delivered into each cell, hence limited in breadth of applications [10].

1.1.3 Chemical delivery method

Chemical approaches, including cationic lipid (lipoplexes) and polycations (polyplexes) mediated transfection [10, 11], are relatively cheap without immune reactions nor many safety concerns, but they suffer from not being quantitative, limiting with cell kinds and delivery molecule selection, as well as poor efficiency [11].

1.1.4 Physical delivery method

Physical approaches involve a wide variety of techniques physically opening holes in the cell membrane [12], including microinjection, gene gun, electroporation, ultrasound treatments, laser irradiation, magnetofection and inkjet printing. Gene gun, in use of particle bombardment or biolistic [13], can achieve high transfection with low amount of molecules (i.e. DNA), but the particles being employed, which are usually gold beads, are expensive, meanwhile toxic and can cause cell damage [14]. Electroporation has been used broadly both in vivo and in vitro for decades, which is characterized as electric field-induced cell membrane permeabilization and / or electrophoretic mobility [15, 16]. Though it is a highly efficient way for cellular molecular delivery, numerous studies have reported large damage and toxicity to cells [15, 17]. Ultrasound treatments, so called sonoporation at low frequencies (e.g. 20kHz) has been shown to enhance the uptake of molecules into cells [18]. Acoustic cavitation is the well-believed mechanism involved in sonoporation, which causes mechanical perturbation and collapse of active bubbles, and the associated energy release can permeabilize adjacent cell membranes [19, 20]. However, cell lysis has been commonly observed accompany with cell membrane permeabilization and molecule uptake [18]. Laser irradiation results in cell membrane permeability modification by a local thermal effect provided by a laser source [21]. But it remains as a relatively novel approach and is not used widely nowadays because of its know-how high-cost and low throughput [11]. Magnetofection is a relatively new method to enhance gene vectors introduction into cells [22], which associates magnetic nanoparticles with gene vectors and promotes uptake into target cells

by an external magnetic field influence. Although magnetofection has been claimed to be economic and high efficient, it is basically an improvement with the same nature as biological delivery method, thus the same limitation exists that transfection reagent toxicity could arouse safety concern [23]. Inkjet printing has recently been reported successfully accomplish cellular transfection process at high cellular viability and low cost by utilizing cell bio-ink and a modified thermal inkjet printer [24]. However, this emerging approach remains to be proven with more demonstration tests.

Microinjection utilizing microneedles stands out of the physical delivery method, which offers precise targeting molecules into nucleus or other desired positions, allowing reproducibly efficient introduction of a wide variety of molecules or structures in a quantitative fashion into single cells, fit for most cell types with high cell viability and function [12, 25-27], without damage nor toxicity.

1.2 Cellular molecular delivery by microinjection

1.2.1 Traditional manual microinjection

Traditional microinjection technique demands for a highly skilled operator to execute the injection operation manually, as shown in Figure 1.1. The operator needs to locate the cell to be manipulated using an optical microscope, and then immobilizes it by aspiration flow from a blunt-tipped micropipette. Then the operator aims the needle at the captured cell and inserts it to implement injection. The micropipette for capture and needle for injection are connected with two manually controlled micromanipulators. After injection, the operator retracts the needle and releases the cell by reversing the aspiration flow direction. It usually takes 2 to 3 months to train an operator to be skillful



Figure 1.1 Manual operation of gene delivery microinjection into living cells.

on the injecting, and even such skillful operators can only finish injection of at most 3 cells per minute, which is quite time-consuming and labor intensive, especially considering that millions of cells manipulations are usually required for our intended applications (e.g. cell therapies). To solve these problems, a lot of studies were inspired to develop automated high throughput microinjection systems.

1.2.2 Semi-automated microinjection systems

Semi-automated microinjection systems with cell array parts have been developed, which are capable to anchor more than 1000 cells at the same time. Bernstein et al. immobilized and positioned embryos into arrays by capillary force, as shown in Figure 1.2 [28], while Sakai et al. applied negative pressure to capture cells onto a silicon plate with multiple holes, as shown in Figure 1.3 [26]. By applying aspiration pressure, a positive pressure can also be used to release the cells from the plate after injection [26], whilst cell release approach in the capillary force system has not been described [28]. When cells are positioned as arrays, PC or CCD cameras were used to control a single needle to implement injection and retraction. Similar systems were improved continually

by many researchers [29-31], which also automatically and robustly identify cell structures for vision-based position control. The cell array design improved cell manipulation speed to some extent (e.g. > 1 cell/s), and such kind of system benefited some applications such as genetic injection into embryos. However, by using single needle to implement injection, the advantage of highly anchoring platform is not fully utilized, and the throughput is hard to be improved further, which is still not satisfied for some applications. Take cell therapy as example, there is no need to identify cell structure before injection, while high-throughput to generate clinically-relevant numbers of cells in a reasonable time frame is the key aspect.

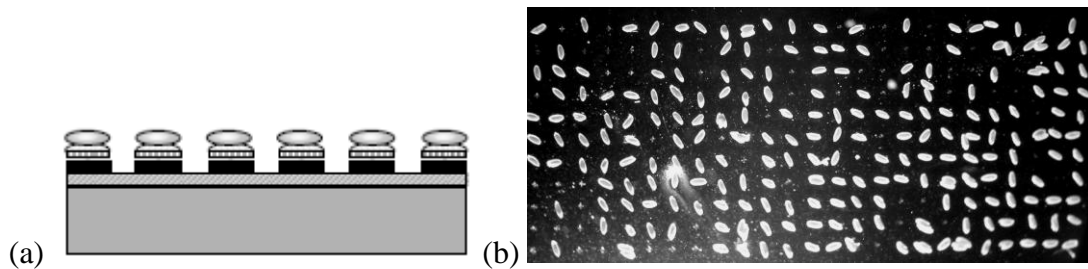


Figure 1.2 Anchoring cells by capillary force [28].

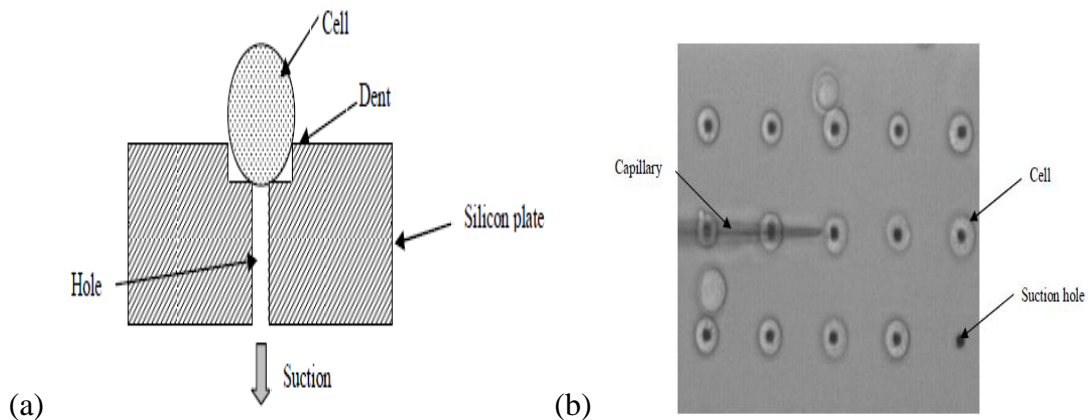


Figure 1.3 Dent structure for cell capturing by aspiration pressure [26].

Besides cell arrays, microneedle arrays has been proposed to improve microinjection throughput, as shown in Figure 1.4 [28]. In 1999, Chun et al. first proposed this idea with fabrication of the array of microcapillaries to implement injection, without elaboration detailed alignment between microneedle array and cell array nor any tests with/without cells [32]. Similarly, Cabodevila et al. produced more intracellular-suitable microneedle arrays to execute injection, but coordination with corresponding cell array nor any tests with/without cells were not shown [33].

1.2.3 Passive automated microinjection

By integrating both of the immobilization and injection functions into one platform, alignment of microinjection array and cell array will no longer be required. Park et al. reported a carbon nanosyringe arrays platform to deliver plasmid and quantum dots into the cytoplasm of cancer cells and human mesenchymal stem cells, as shown in Figure 1.5 [34]. The system uses an amphiphilic polymer to enable loading of cargo into the hollow cores of the tubular carbon nanosyringes, and seeds cells onto the syringes and get pierced in a spontaneous manner by cells' own gravity. The loading cargo will be dispersed into the cell in an aqueous solution. Similar studies include immobilization and injection using carbon nanofiber arrays and self-assembled monolayers [35, 36]. However, the way to load cargo is hard to control, and capturing / piercing cells by their own gravity is not reliable. Finally, it is unclear whether cells could be easily released and collected from such arrays, which would be required in many applications (e.g. cell-based therapies).

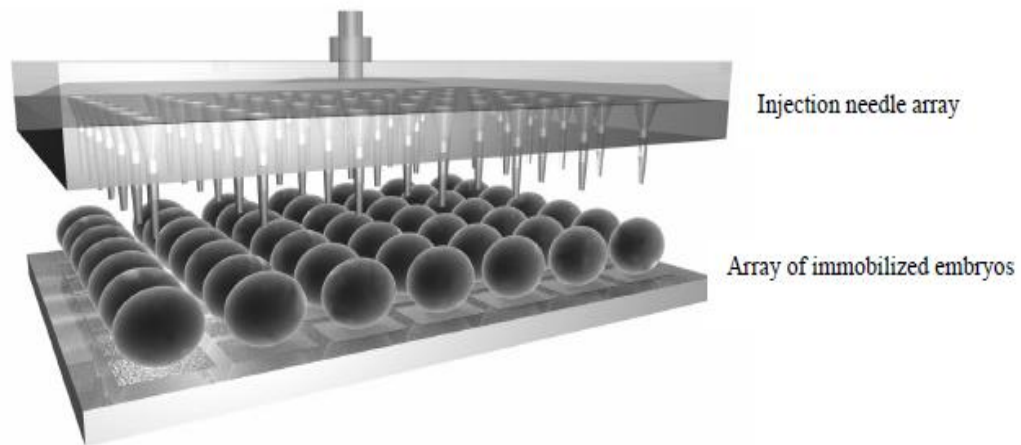


Figure 1.4 A schematic drawing of the proposed concept for a high-throughput microinjection system using both microneedle arrays and cell arrays [28].

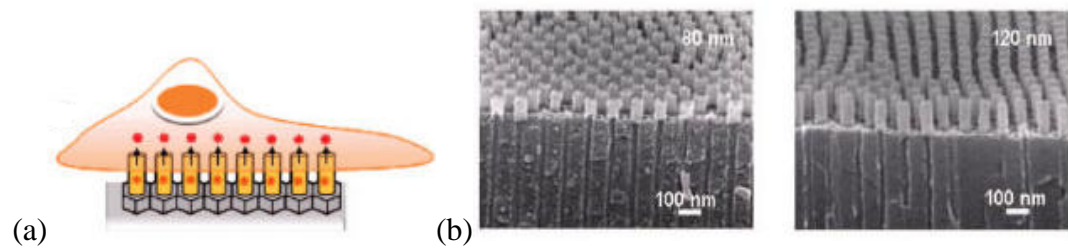


Figure 1.5 a) Schematic of carbon nanosyringe arrays with cell seeding; b) SEM images of carbon nanosyringe arrays with exposed heights of 80 nm and 120 nm [34].

1.2.4 Microfluidic manner based automated cell injection system

Adamo and Jensen described a disposable microfluidic device for low cost, quantitative microinjection in which the usual microinjection strategy is reversed. Cell injection is achieved by moving cells onto a stationary microneedle instead of moving the needle into an immobilized cell, as shown in Figure 1.6 [25]. In an operation cycle, the

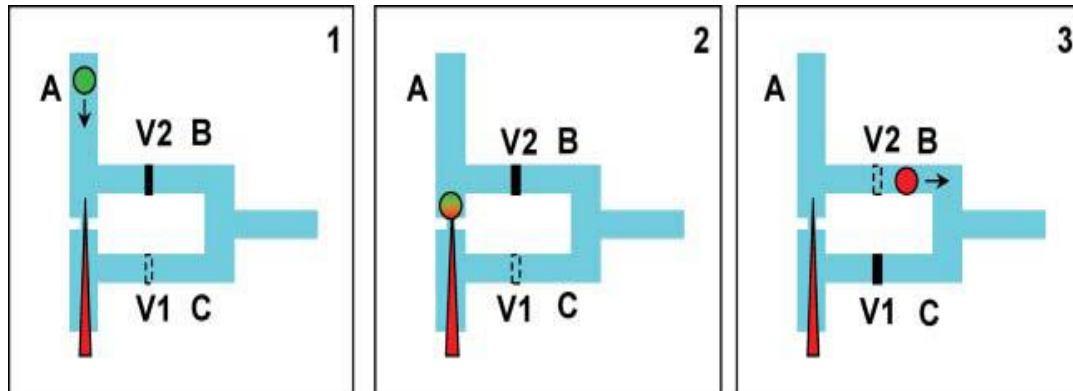


Figure 1.6 Schematic representation of the microfluidic manner based automated single cell microinjection system [25].

cell coming from a supply reservoir is transported towards the needle along channel A by fluidic stream draining through channel C with channel B closed. After being pierced and injected, channel C is closed and channel B is open. Reverse flow generated by the actuation of valve V2 lifts the cell off the needle and carries the injected cell to a collection reservoir. As a rough conservative estimate, the system would be able to perform at least one cell injection per second [25], which is more efficient than manual manipulation, but is still unsatisfied for many applications.

1.3 Dissertation outline

In this dissertation, we will present a new cellular molecular delivery device by utilizing mechanoporation, which is a massively-parallelized MEMS-based platform for passively delivering molecules into living cells via mechanical cell membrane penetration. The new device is aimed to minimize necessary human interaction and achieve ultrahigh throughput (UHT) to generate clinically-relevant numbers of cells, with reliable and

robust cell delivery, capture, penetration and release approaches. It is also an interim device, which represents key steps towards our long-term goal to realize UHT active microinjection device, and at the same time provides utility in and of itself.

This following dissertation is divided into 5 chapters. Chapters 2, 3 and 4 will discuss our new device design, fabrication and validation respectively. Chapter 5 will propose our future directions to improve the system and realize UHT active microinjection system. Chapter 6 is the conclusion of the dissertation.

2. Instrumentation Design

Microinjection technology is considered the gold standard for cellular manipulation, because of its precision, safety and applicability for a wide variety of cell types and molecules. To overcome limitations of traditional manual operation, automated and high-throughput microinjection-based cellular manipulation has been studied extensively, as discussed in the preceding chapter. However, there is still great potential to improve instrumentation to allow fully-automated and higher throughput microinjection of cellular molecular delivery, in order to satisfy needs for cell-based-therapies, as well as other applications currently limited by prevailing manipulation techniques. A new instrumentation capable of simultaneous capturing and piercing of many thousands of cells within minutes is developed.

2.1 Instrumentation concept

As shown in Figure 2.1, a proposed instrumentation, so called UHT active microinjection device, integrates functions of cell capture, injection and releasing into a single device chip, where the injectors are within capture sites. During operation procedure, cells will be introduced onto the Capture & Injection Site Array. Then they will be captured using negative aspiration flow. Uncaptured cells will be washed away, while maintaining low-rate negative aspiration flow to hold captured cells, so that only permeabilized cells are collected and analyzed after injection. Once finishing injection, the permeabilized cells will be released from the Capture & Injection Site Array by positive aspiration flow, following with collection. The monolithic integration of all

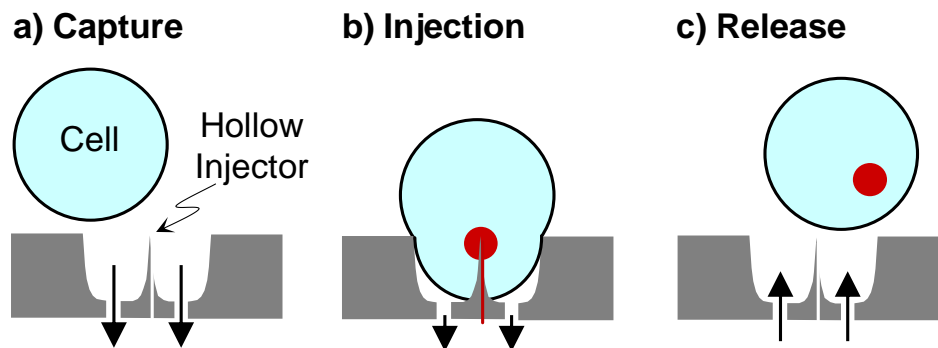


Figure 2.1 Schematic of a proposed UHT active microinjection instrumentation concept. Arrows denote flow direction and magnitude.

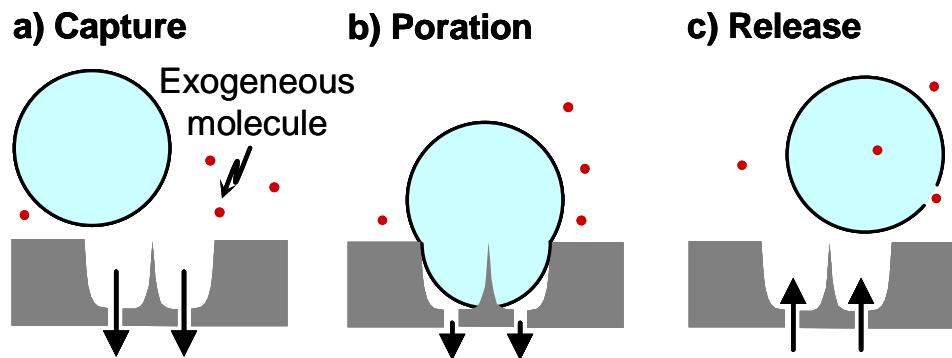


Figure 2.2 Schematic of the proposed UHT mechanoporation instrumentation concept. Arrows denote flow direction and magnitude.

functionalities within in a single chip enables considerable simplification relative to robotic serialized microinjection instrumentation, while massive parallelization offers opportunity for throughputs many orders of magnitude greater than the current state-of-the-art.

In terms of predictable complexity and enormous difficulty to realize the UHT active microinjection device, we first turn into developing an interim device that

represents a key step towards UHT active microinjection, as shown in Figure 2.2. In this device, the hollow injectors are replaced with solid penetrators. This interim device simplifies design and fabrication considerably, thus allowing expedited evaluation of key aspects of concept feasibility. Moreover, this design provides utility in and of itself, since it enables cellular manipulation via UHT mechanoporation, i.e. mechanical membrane disruption enables transfection into live cells via diffusive influx of exogenous molecules from the surrounding suspension.

2.2 Device design

The UHT mechanoporation device is a 15 by 15 mm chip, which consists of a 100 x 100 array of Capture Sites monolithically integrated 0.5 μm - tip size Solid Penetrators,

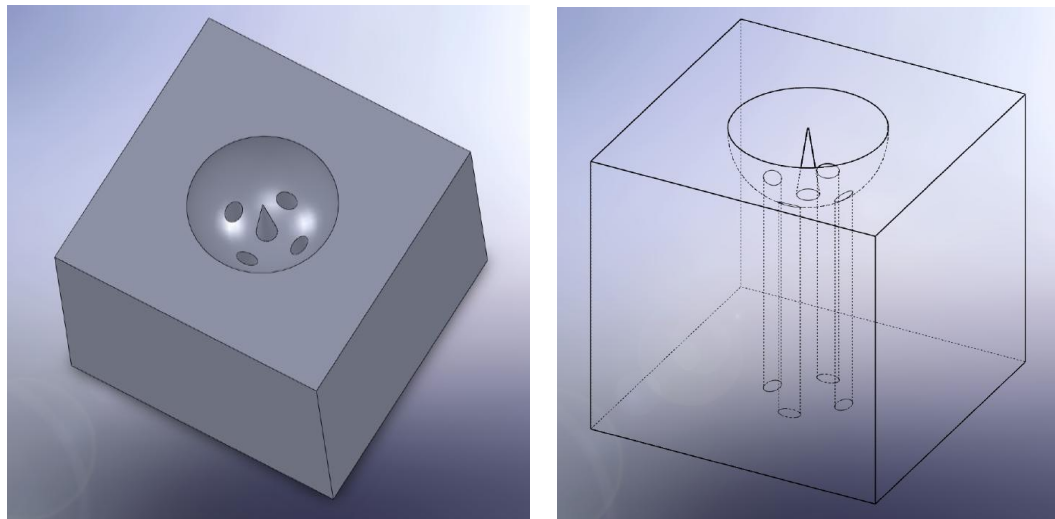


Figure 2.3 Schematics of single UHT mechanoporation instrument Capture Site monolithically integrated with solid penetrator, and four elliptical aspiration vias at the bottom, which are connecting with aspiration port.

as shown in Figure 2.3, to yield capability for simultaneous manipulation of maximum 10^4 cells per capture cycle. The Capture Site is designed to be a $16\ \mu\text{m}$ diameter hemisphere, based on the size of cells to be manipulated (K652 cells and Mouse Embryo Fibroblast (MEF) cells in this study). Each Capture Site contains four $2\ \mu\text{m}$ by $4\ \mu\text{m}$ elliptical Aspiration Vias located at the bottom. As will be discussed later, the choice of elliptical vias is dictated by the desire to produce roughly hemispherical Capture Sites via isotropic etching through the vias. Use of multiple vias in Capture Site will provide uniform tension on the cell membrane to facilitate capturing and penetration.

2.3 Operation parameter estimation

2.3.1 Cell membrane penetration force estimation

Using negative aspiration flow through the four vias within each Capture Site, cells can be not only captured, but also pierced by the Solid Penetrators. Several studies reported penetration pressure for different cells and various injectors, e.g., about 32 kPa is enough to pierce human epidermal melanocyte cells using 200 nm-diameter pyramidal Si tips [37]; 74 kPa is sufficient to penetrate drosophila embryos using $30\ \mu\text{m}$ -diameter silicon nitride needle [38], etc. Adamo and Jensen used similar size cells as we will use in our study and claimed that cell speed in the range of 0.3-3 mm/s are adequate to impart enough momentum for the cell to achieve piercing by $0.5\ \mu\text{m}$ -diameter glass capillaries [25], which is also the same size level penetrator as we are going to create.

To better understand cell membrane penetration process by mechanical piercing, force sensors are used to measure forces applied to cells [5, 39-41]. Without experimental

measurement, it is next to impossible to accurately analyze the needed force to penetrate the cell membrane either theoretically or numerically, since reliable data on the individual subcellular rheology and its contraction with other parts are lacking [42]. Some research groups developed several cell mechanical models based on membrane theory to characterize cell mechanical properties and responses in mechanical piercing [39, 41-44]. However, only cell membrane deformation was shown to be simulated during indentation, while cell membrane rupture at the piercing moment was not able to be modeled. In general, the failure mechanism of cell membrane, including the failure strain and stress when penetration occurs cannot be predicted, and the loading force to induce a penetration is unable to anticipate without experimental measurement.

To get a clue of the needed penetration force, a feasible but imprecise way is to compare the parameters from other research studies in the related field, which provided both cell membrane mechanical property data and mechanical piercing conditions with penetration forces measured, and scale down those parameters to our specific situations to coarsely estimate the needed penetration force. As shown in Table 2.1, cell types and corresponding cell membrane mechanical property parameters, as well as cell membrane rupture forces and injector sizes are listed. In our specific applications, K562 cells and MEF cells are going to be used for device cell tests.

For K562 cells, very few references were found providing their cell membrane mechanical properties, except one mentioned that their elastic modulus is about 0.03 kPa [45]. It is known that our injector tip size is about $0.5 \mu m$, and the cell diameter is about $15 \mu m$, and we assume, for the purposes of this preliminary estimation exercise, that the

penetration force is in linear relationship with the cell membrane elastic modulus, when the ratio between injector tip size and cell diameter is comparable in different situations. Thus based on data from Sun's group about mouse oocyte ZP [39] as shown in Table 2.1, the force to penetrate K562 cell membrane is calculated to be about 12.6 nN, as shown in Figure 2.4. Since the penetration force is implemented by the pressure drop along the aspiration vias on the cell membrane, the pressure drop along our device aspiration vias is calculated as:

$$\Delta P = \frac{F}{4A} = \frac{F}{4\pi ab} \quad (2.1)$$

where F is the penetration force, A is the single aspiration via area, a is the elliptical via's semi-minor axis dimension, b is the elliptical via's semi-major axis dimension. ΔP is calculated to be 0.5 kPa .

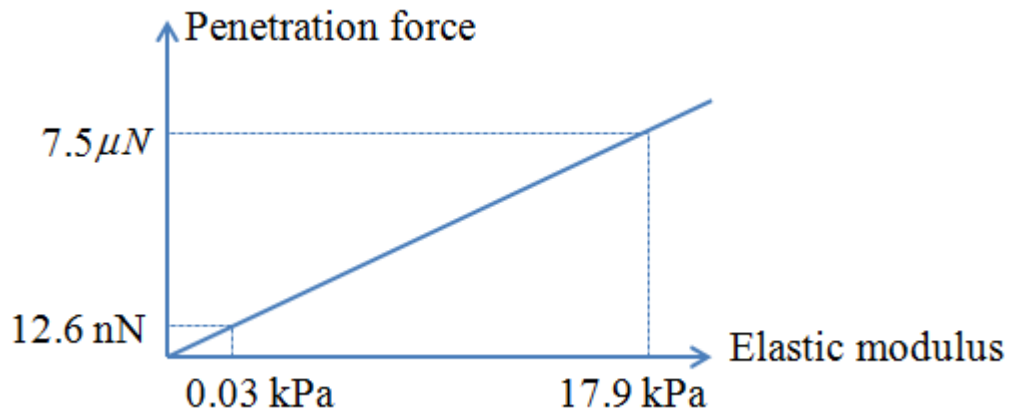


Figure 2.4 Schematics of penetration force in linear relationship with elastic modulus in the condition of K562 cell membrane penetration force calculation.

Table 2.1 List of cell types, cell membrane mechanical properties, cell membrane penetration forces and injector tip sizes from other research studies.

Reference	Injector tip size	Cell Type	Cell membrane mechanical properties	Cell membrane penetration force
Y.Sun, et al. 2003 [39]	3 μm	Mouse oocyte ZP (zona pellucid)	Diameter: 52-61 μm Thickness: 4.5 μm Elastic modulus: 17.9 kPa Poisson ratio: 0.5	Puncture force: 7.5 μN
		Mouse embryo ZP(zona pellucid)	Diameter: 52-61 μm Thickness: 4.5 μm Elastic modulus: 42.2 kPa Poisson ratio: 0.5	Puncture force: 13 μN
Y.Tan, et al. 2008 [41]	7.5 μm	Zebrafish embryos	Diameter: 500 μm Thickness: 3 μm Elastic modulus: 1.04 MPa	Puncture force: 784 μN
	12.5 μm	Medaka embryos	Diameter: 600 μm Thickness: 22 μm Elastic modulus: 2.83 MPa	Puncture force: 12450 μN

Our manipulated cell solution is diluted, and can be treated as water at room temperature $25^{\circ}c$, whose dynamic viscosity is $\mu = 8.94 \times 10^{-4} Pa \cdot s$. By also assuming that the negative aspiration flow is Newtonian laminar flow, fully developed and steady, governed by Poiseuille law, which is adjusted for elliptical via cross section, as shown in Figure 2.5, the flow field governing equation is:

$$\frac{\partial^2 w}{\partial x^2} + \frac{\partial^2 w}{\partial y^2} = \frac{1}{\mu} \frac{\partial P}{\partial z} \quad (2.2)$$

where $w(x, y)$ is the flow velocity function. By applying boundary condition that $w(x, y) = 0$ at the elliptical via's circum, $w(x, y)$ can be obtained as:

$$w(x, y) = -\frac{\partial P}{\partial z} \cdot \frac{1}{2\mu} \cdot \frac{a^2 b^2}{a^2 + b^2} \left(1 - \frac{x^2}{a^2} - \frac{y^2}{b^2}\right) \quad (2.3)$$

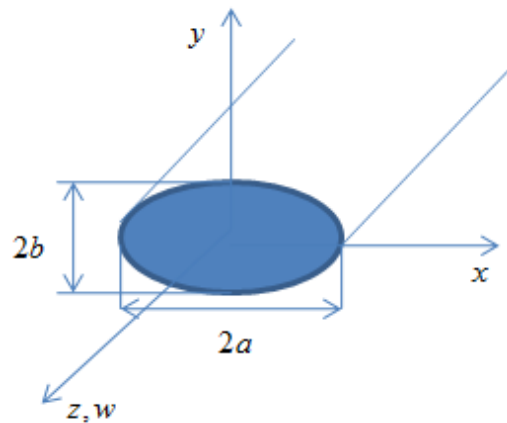


Figure 2.5 Schematics of elliptical aspiration via's cross section in coordinate system to calculate flow velocity flowing through the via in z direction.

where $\frac{\partial P}{\partial z}$ is simplified as $\frac{\Delta P}{L}$, ΔP is the pressure drop obtained from equation (2.2),

L is the aspiration via's length. Thus flow rate q flowing into each aspiration via is:

$$q = \int_A w dA = w(0,0) \cdot \frac{\pi}{2} ab \quad (2.4)$$

And flow speed, which is also cell solution speed above each capture well is:

$$V = \frac{4q}{A_{capturewell}} \quad (2.5)$$

which is 0.59 mm/sec in this case, and corresponding aspiration flow rate into the entire aspiration circuit is about $140 \mu\text{L/min}$, to have the K562 cell membranes being penetrated.

For the MEF cells, a measured mean penetration force was found [40] to be $2.9 \pm 1.9 \mu\text{N}$ by using a $60 \mu\text{m}$ -diameter glass indenter. Also we assume for the purposes of

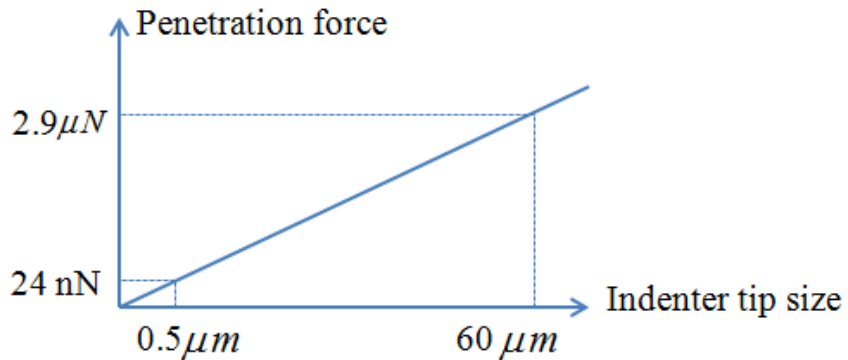


Figure 2.6 Schematics of penetration force in linear relationship with indenter's tip size in the condition of MEF cell membrane penetration force calculation.

this preliminary estimation exercise, that penetration force is in linear relationship with the indenter's tip size, the force to penetrate MEF cells with our $0.5 \mu\text{m}$ -tip penetrators is about 24.2 nN, as shown in Figure 2.6. With the same cell solution assumptions as described for K562 cells above and equations 2.1-2.5, the pressure drop along our device aspiration vias should be about 0.96 kPa. Cell solution speed is about 1.12 mm/s, and the corresponding cell solution flow rate into the entire aspiration circuit is about $270 \mu\text{L}/\text{min}$, for achieving MEF cell membrane mechanical piercing.

2.3.2 Cell speed estimation

Noticing that in the above section, it is the cell solution speeds that have been calculated, and corresponding cell speeds are demanded so that we can compare our estimation results with Adamo and Jensen's study [25]. To calculate cell speeds, single cell is treated as rigid sphere moving along the axis of a tube (as denoted in x direction) in Poiseuille flow, where the stream function ψ is [46]:

$$\psi = \psi^P + s_x \psi^{3D-ST-x} + d_x \psi^{3D-PSD-x} \quad (2.6)$$

where ψ^P is the stream function of unperturbed parabolic Poiseuille flow in a cylindrical tube without sphere; s_x and d_x are two constant coefficients; $\psi^{3D-ST-x}$ is the stream function of flow due to a point force; and $\psi^{3D-PSD-x}$ is the stream function of irrotational flow due to a 3D point-source dipole pointing in the direction of the x-axis. Applying appropriate boundary conditions, the single cell speed U can be expressed in the following equation:

$$U = U_{\max}^P \left(1 - \frac{2a^2}{3b^2}\right) - \frac{F_x}{6\pi\mu a} \quad (2.7)$$

where U_{\max}^P is the unperturbed parabolic Poiseuille flow axial speed; a is the cell radius; b is the cylindrical tube radius; μ is the flow dynamic viscosity; and F_x is the hydrodynamic force exerted on the sphere, which can be expressed as $F_x = -\frac{4}{3}\pi a^3(\rho_s - \rho)g$ when assuming that the cell is moving under steady speed. Equation (2.2) is strictly valid for a sphere that is immersed in infinite parabolic flow with / without the tube wall while Re is small [46].

For our cell speed estimation, constants in equation (2.2) are listed in Table 2.2. Comparing with the solid Penetrator array's size, single cell can be treated as a sphere that is immersed in infinite parabolic flow, while surrounding cell solution speed can be assumed as same as the unperturbed parabolic Poiseuille flow axial speed. According to cell solution speeds, 0.59 mm/s for K562 cells and 1.1 mm/s for MEF cells obtained in the previous section, cell speeds are calculated to be 0.59 mm/s for K562 cells and 1.1 mm/s for MEF cells respectively, which agree with Adamo and Jensen's conclusion [25].

Table 2.2 Constants in equation (2.2) for cell speeds calculation.

Cell density ρ_s (kg / m ³)	Dynamic viscosity μ (Pa · s)	Cell radius a (μ m)	Cylindrical tube radius b (μ m)
1.4×10^3	8.94×10^{-4}	5	100

2.3.3 Pressure drop and cell solution speed numerical simulation

The resulted pressure drops along the device aspiration vias, 0.5 kPa for K562 cells and 0.96 kPa for MEF cells obtained in section 2.3.1 respectively, are comparable to or much less than other aspiration-based capture devices using similar cell sizes, none of which reported detrimental effect on captured cells [26, 47]. It is also well below the 527 kPa failure pressure estimated for a comparable solid membrane using the analyses developed by van Rijn and Elwenspoek [48].

To further verify those analytical calculation results, numerical simulation using Comsol (v3.3 & v4.2) was conducted to study flow field and pressure field with / without cell being captured by the solid penetrator in a single capture well. For simplification, both K562 cell and MEF cell sizes are assumed to be 10 μm in diameter in the simulation. Figure 2.7-2.10 show steady-state Newtonian laminar flow field and pressure field adjacent to single Solid Penetrator and in vias.

Figure 2.7 shows that, during K562 cell transportation before cell being captured on solid penetrator, with 0.5 mm/s cell solution velocity above the solid penetrator, the maximum flow velocity in the vias is about 17.2 mm/s, as it is about 18.6 mm/s with analytical calculation (about 7.5% deviation). And the simulated pressure drop in this condition is about 0.53 kPa, which is very close to the analytical calculation result (about 6% deviation).

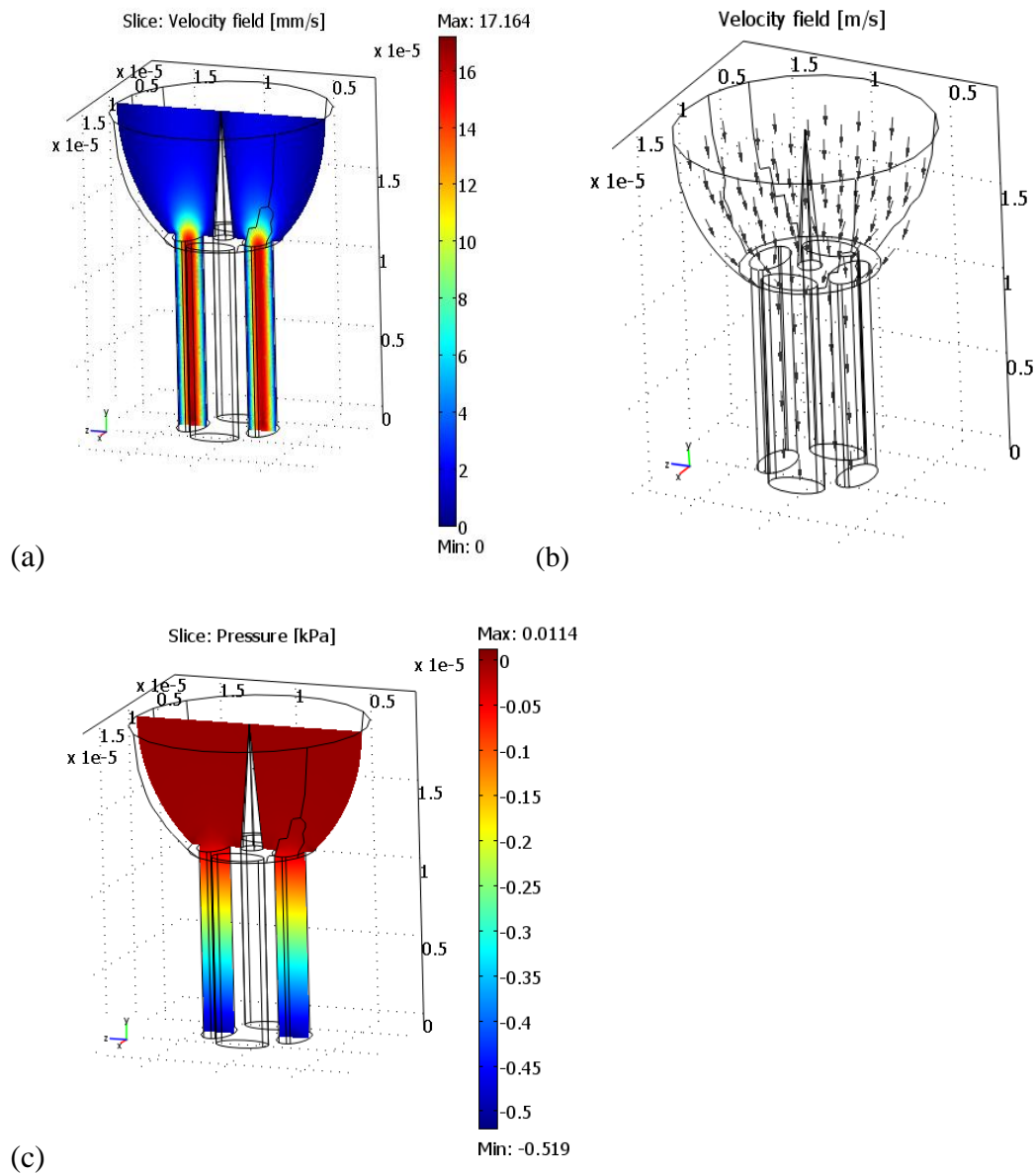


Figure 2.7 Numerical simulation results of (a) velocity magnitude field (b) velocity vector field and (c) pressure field adjacent to Solid Penetrator and in vias, under steady state condition during K562 cell transportation before cell being captured on Solid Penetrator.

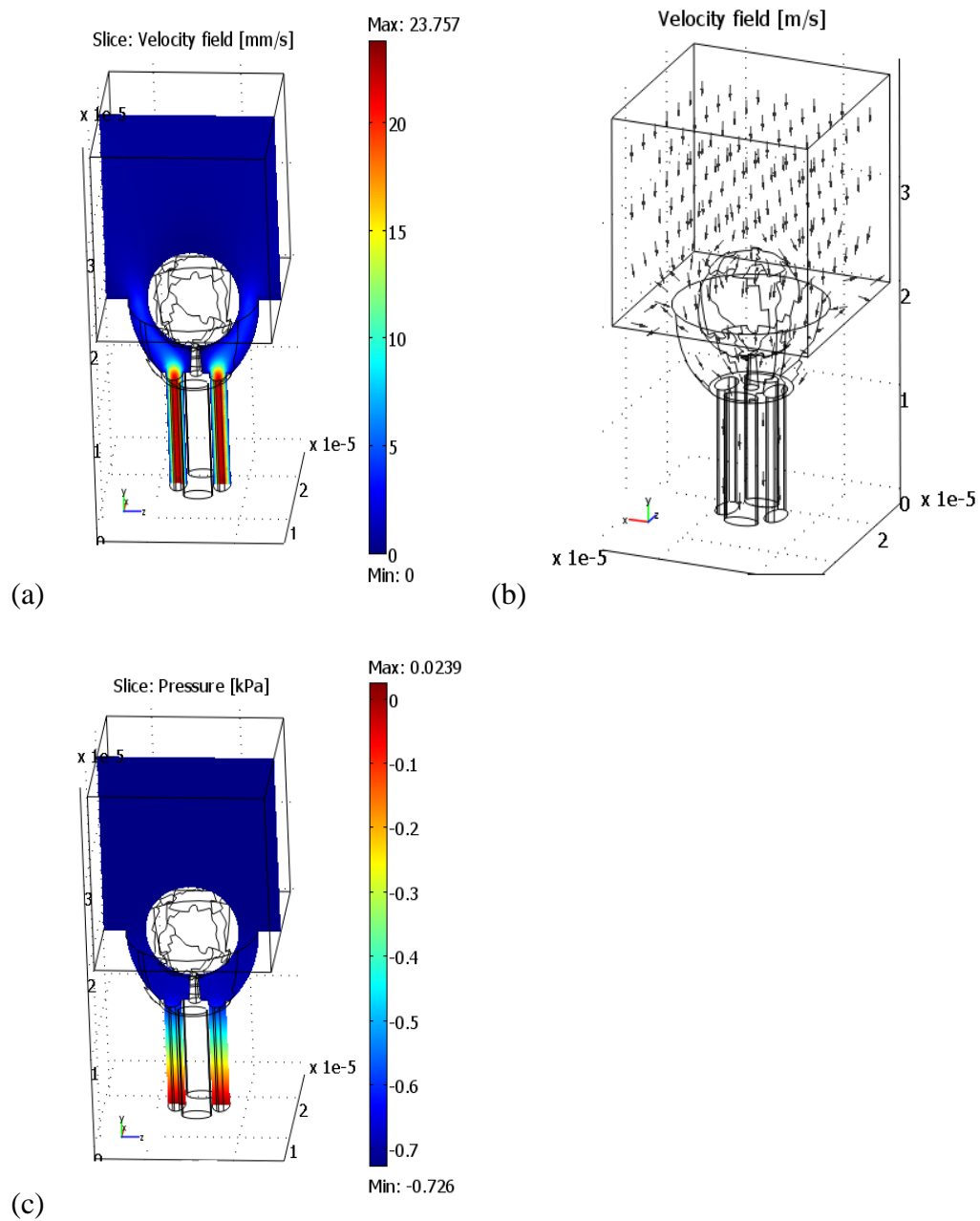


Figure 2.8 Numerical simulation results of (a) velocity magnitude field (b) velocity vector field and (c) pressure field adjacent to Solid Penetrator and in vias, under steady state condition at the moment that K562 cell is captured on Solid Penetrator.

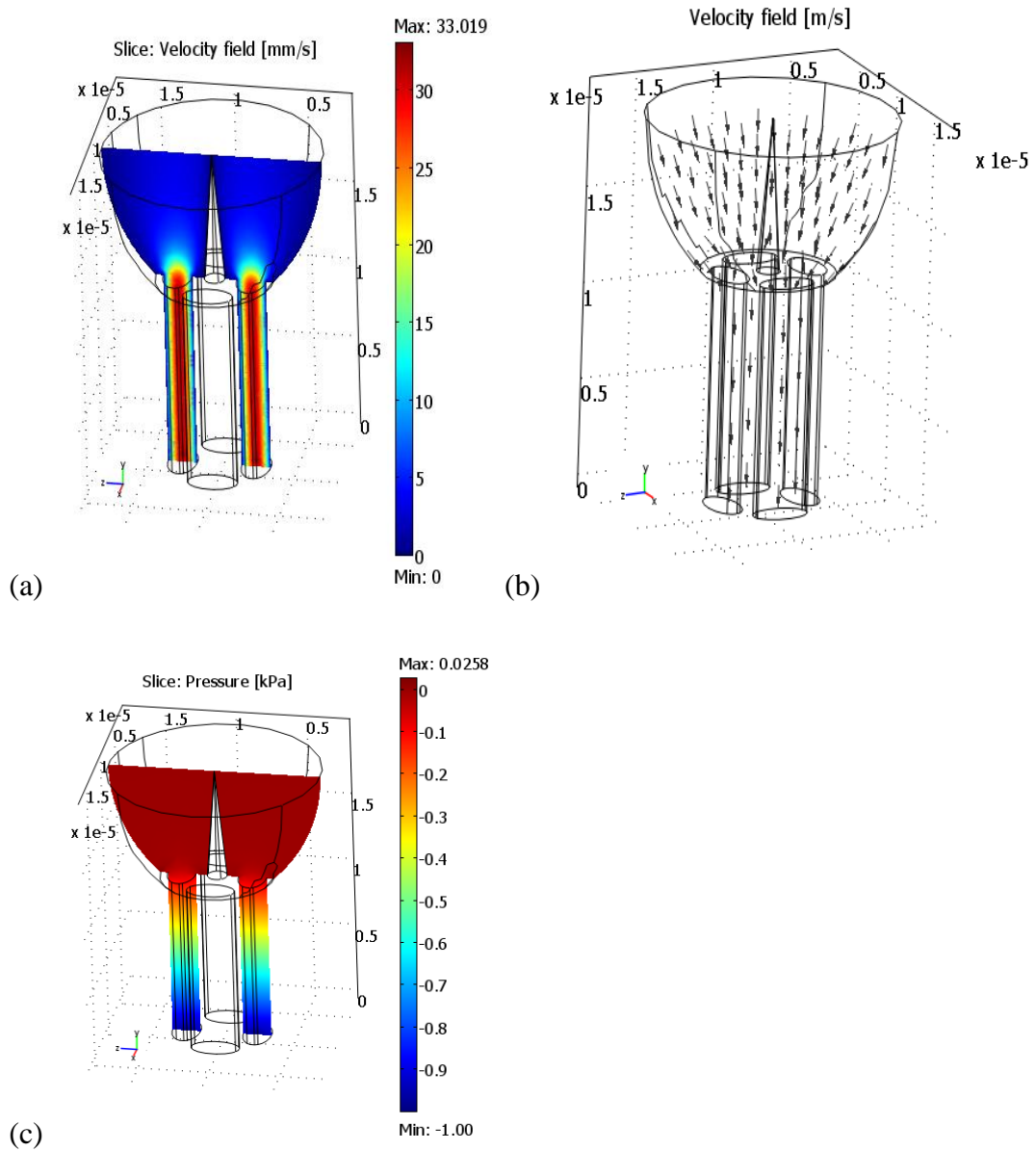


Figure 2.9 Numerical simulation results of (a) velocity magnitude field (b) velocity vector field and (c) pressure field adjacent to Solid Penetrator and in vias, under steady state condition during MEF cell transportation before cell being captured.

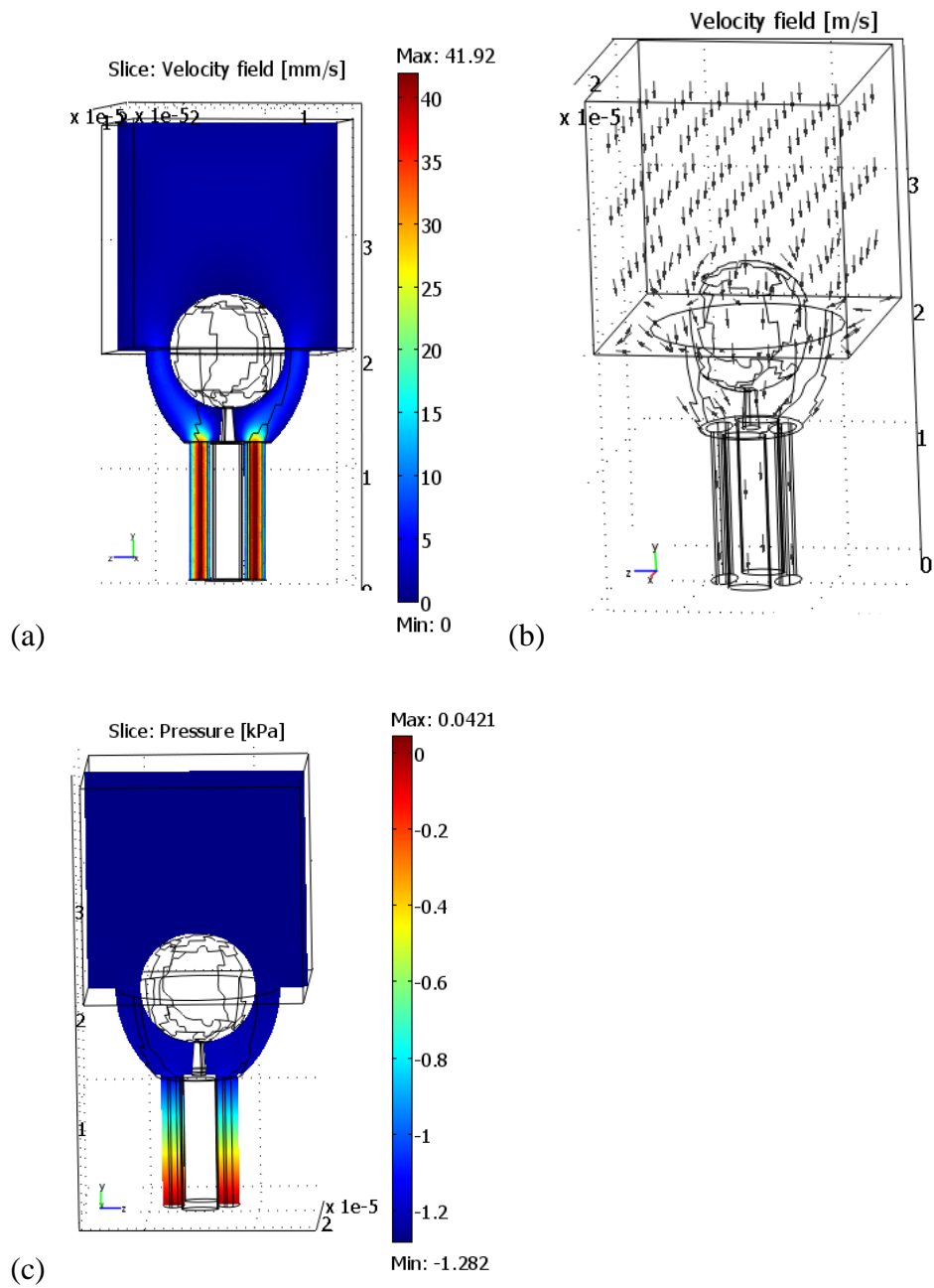


Figure 2.10 Numerical simulation results of (a) velocity magnitude field (b) velocity vector field and (c) pressure field adjacent to Solid Penetrator and in vias under steady state condition after MEF cell being captured on solid penetrator.

Figure 2.8 shows that, at the moment that K562 cell being captured on Solid Penetrator with 0.5 mm/s cell solution velocity, the maximum flow velocity in the vias is about 23.8 mm/s, increasing 38% than the flow velocity when without cell being captured. And the simulated pressure drop in this condition is about 0.75 kPa, increasing 41% than the pressure drop when without cell being captured.

Figure 2.9 shows that, during MEF cell transportation before cell being captured on Solid Penetrator with 1.12 mm/s cell solution velocity, the maximum flow velocity in the vias is about 33 mm/s, as it is about 36 mm/s with analytical calculation (about 8.3% deviation). And the simulated pressure drop in this condition is about 1 kPa, which is very close to the analytical calculation result 0.96 kPa (about 4% deviation).

Figure 2.10 shows that, at the moment MEF cell being captured on Solid Penetrator with 1.12 mm/s cell solution velocity, the maximum flow velocity in the vias is about 43.6 mm/s, increasing 32% than the flow velocity when without cell being captured. And the simulated pressure drop in this condition is about 1.37 kPa, increasing 37% than the pressure drop when without cell being captured.

2.3.4 Conclusion

Though the assumption of linear relationship between penetration force and cell membrane elastic modulus, as well as between penetration force and indenter's tip size in section 2.3.1 are crude and fail to account for the non-linear, viscoelastic nature of the cells, under current circumstances that related studies have barely been done, we predict that the device operation parameters are within the expected and reasonable range, and

the device design is performable. The section 2.3 provides methods to initially verify the device concept and design, which also provides data to support the cell tests after device fabrication completed, which will be shown in Chapter 4.

3. Device Fabrication

The majority of the device microfabrication and characterization effort described below was performed in the University of California – Riverside (UCR) Center for Nanoscale Science and Engineering (CNSE) Nanofabrication Cleanroom Facility, University of California - Irvine (UCI) Integrated Nanosystems Research Facility (INRF) and University of California – Santa Barbara (UCSB) Nanotech Nanofabrication Facility. Conventional silicon micromachining techniques were utilized.

The microfabrication and characterization procedure includes 5 key steps, as presented below and shown in Figure 3.1. A single 100 mm diameter silicon-on-insulator (SOI) substrate with 20 μm Si device layer, 2 μm buried SiO_2 (BOX) layer and 500 μm Si handle layer (Ultrasil Corporation) is used.

In step 1, a layer of 1 μm SiO_2 mask is deposited on both sides of the SOI substrate using thermal oxidation (CVD Equipment oxidation furnace, UCR). The film thickness is verified using Spectroscopic Phase Modulated Ellipsometer (Uvisel FUV 200, UCR). Another 2 μm SiO_2 mask is deposited on handle layer of the SOI substrate using Plasma Enhanced Chemical Vapor Deposition (PECVD) (Unaxis / Plasma Therm 790, UCR).

The following is the detailed process flow outlining the microfabrication procedures of step 1:

(1) Thermal oxidation of both sides of the 4 inch SOI wafer

- 7 sccm H₂, 4 sccm O₂, at 1100 °c
- 2 hours, average SiO₂ film thickness ~ 1 μm

(2) PECVD deposit SiO₂ film on handle layer of SOI wafer

- 900 mTorr, 400 sccm 2% SiH₄, 900 sccm N₂O, and 25 W power
- 50 minutes, average film thickness ~ 2 μm

In step 2, the elliptical vias is patterned on the device layer of the SOI substrate

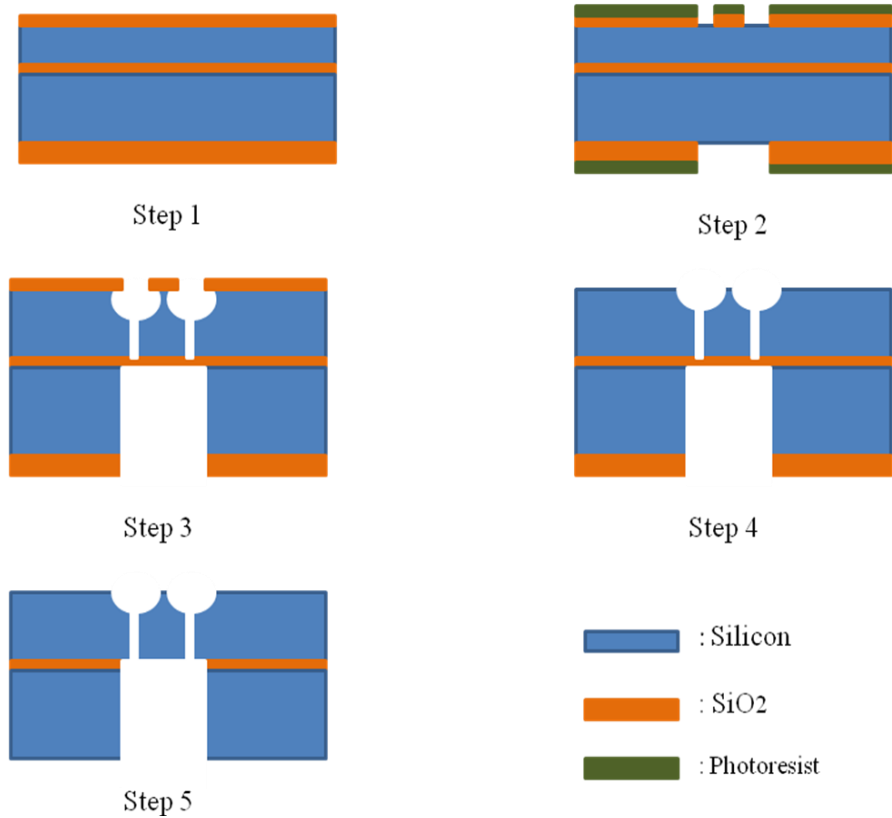


Figure 3.1 Device microfabrication process flow. Only one Capture Site is shown for the sake of clarity.

using projection (stepper) lithography (GCA 6300 i-line system, UCSB). The aspiration ports connecting the vias on the handle layer of the SOI substrate is patterned using alignment contact lithography (Suss Micro Tec MA6 MA6 contact aligner system, UCSB). All the patterns are transferred from photoresist to SiO₂ mask layer by CF₄ / CHF₃ dry etching (STS Multiplex RIE, UCR).

The following is the detailed process flow outlining the microfabrication procedures of step 2:

(1) Projection (stepper) lithography, device layer of SOI wafer – elliptical vias

- Using SPR 955 CM-0.9 positive photoresist
- Apply HMDS and spin
- Apply resist and spin 3000 rpm for 30 sec
- 60 sec pre-exposure bake at 95 °C
- Exposure for 1.6 sec
- 60 sec post-exposure bake at 110 °C
- Develop in MIF 300 for 70 sec

(2) SiO₂ mask etching- transfer patterns into SiO₂ mask from photoresist

- 300 W Power, 100 mTorr pressure, 30 sccm CHF₃ and 20 sccm CF₄
- ~ 5 min etch

(3) Contact lithography, handle layer of SOI wafer- big aspiration port

- Using SPR 220-3.0 positive photoresist
- Apply HMDS and spin
- Apply resist and spin 2000 rpm for 40 sec
- 90 sec pre-exposure bake at 115 °C
- Exposure for 20 sec
- 90 sec post-exposure bake at 115
- Develop in AZ300MIF for 60 sec

(4) SiO₂ mask etching- transfer patterns into SiO₂ mask from photoresist

- 300 W Power, 100 mTorr pressure, 30 sccm CHF₃ and 20 sccm CF₄
- ~ 15 min etch

In step 3, the aspiration port is extended to BOX layer using silicon deep reactive ion etching (DRIE) process (STS MESC ICP Etcher, UCI), which is also known as Bosch Process [49, 50]. The process consists of sequential SF₆ etching and C₄F₈ passivation steps. The Capture Sites monolithically integrated Solid Penetrators are produced by isotropic etching through the elliptical vias on device layer (STS MESC ICP Etcher, UCI), which is a process from modified Bosch Process without C₄F₈ passivation step. The aspiration vias are then extended to BOX layer by an anisotropic etching (STS MESC ICP Etcher, UCI) from modified Bosch process with shorter SF₆ etching and C₄F₈ passivation steps. Then SiO₂ mask layer on device layer is removed by CF₄ / CHF₃ dry etching (STS Multiplex RIE, UCR).

The following is the detailed process flow outlining the microfabrication procedures of step 3:

(1) DRIE – aspiration port on handle layer

- Etching step: 700 W ICP coil power, 20 W platen power, 37 mTorr pressure, 130 sccm SF₆, 13 sccm O₂, 14 sec
- Passivation step: 600 W ICP coil power, 0 W platen power, 28 mTorr pressure, 85 sccm C₄F₈, 7 sec
- ~ 2 hour 20 min etch

(2) Clean samples (UCR): Piranha, mixture of H₂SO₄ (96% concentration) and H₂O₂ (30% concentration), ratio 1:1, ~30 min.

(3) Verification of elliptical vias' feature size and uniformity using SEM (Scanning Electron Microscope) (Leo SUPRA 55 system, UCR), as shown in Figure 3.2.

(4) Silicon isotropic etching- capture wells and Solid Penetrators on device layer

- 500 W ICP coil power, 20 W platen power, 12 mTorr pressure, 95 sccm SF₆, 13 sccm O₂
- ~ 4 min 10 sec etch

(5) Verification of capture wells and Solid Penetrator tops feature size and uniformity using Optical Microscope (UCI), as shown in Figure 3.3.

(6) DRIE – aspiration vias on device layer

- Etching step: 600 W ICP coil power, 17 W platen power, 22 mTorr pressure, 130 sccm SF₆, 13 sccm O₂, 7 sec
- Passivation step: 600 W ICP coil power, 0 W platen power, 16 mTorr pressure, 85 sccm C₄F₈, 5 sec
- ~ 11 min etch

(7) SiO₂ mask removal dry etching- device layer

- 300 W Power, 100 mTorr pressure, 30 sccm CHF₃ and 20 sccm CF₄
- ~ 4 min 30 sec etch

(8) Verification of capture wells and Solid Penetrator feature size and uniformity using SEM (Leo SUPRA 55 system, UCR), as shown in Figure 3.4.

In step 3, the vias feature (verticality, smoothness, etc.) is not characterized every time since Focused Ion Beam Milling (FIB, UCR) would be needed to cut the device chip and present a single via's cross section, which will result in useless of the device chip. However, the recipe to produce vias as shown in step 3-(6) was developed based on FIB (Leo XB1540 system) verification, as shown in Figure 3.5. Since the STS MESC ICP Etcher always functions consistently, we assume that the vias are fabricated as expected every time.

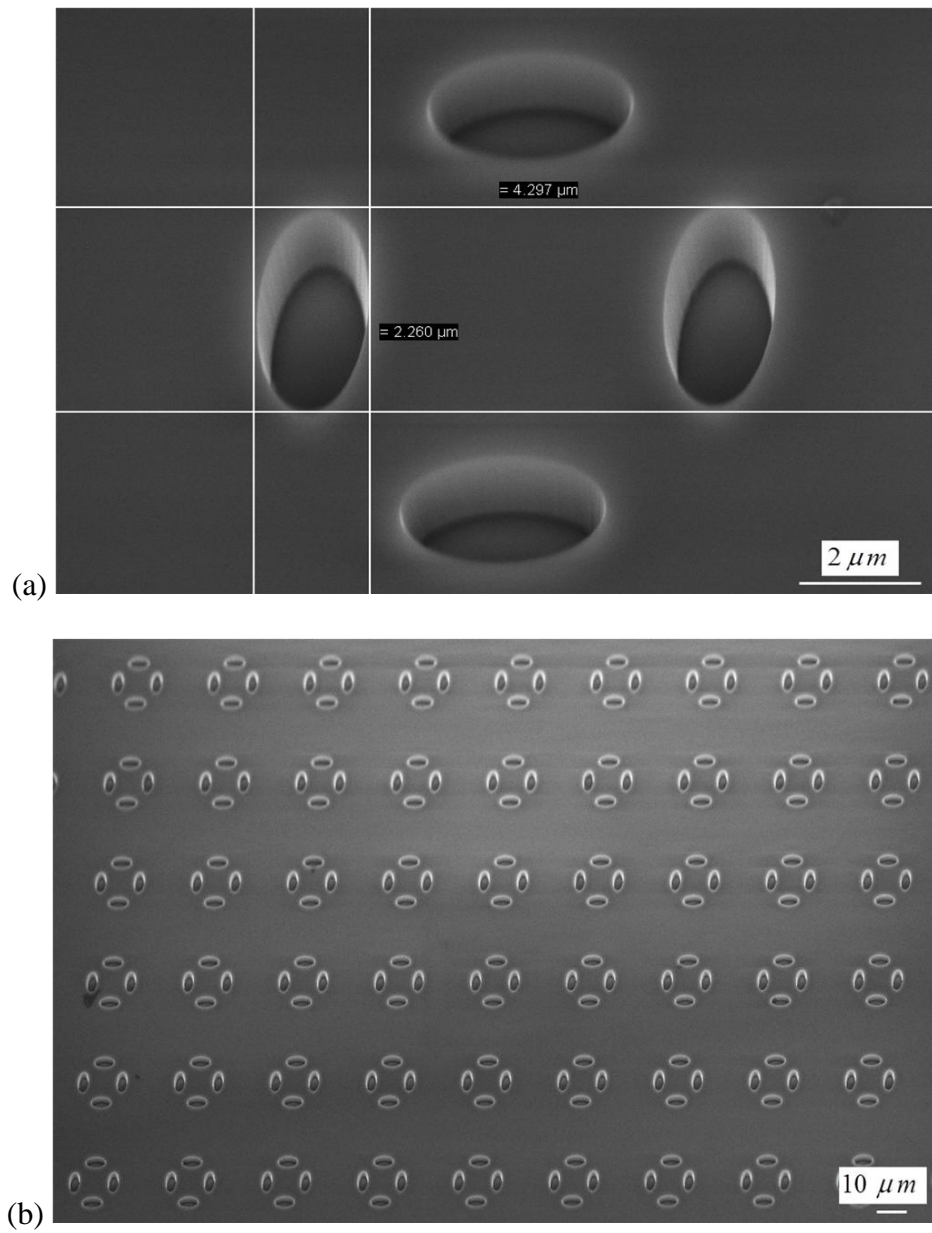


Figure 3.2 SEM images of elliptical via patterns. (a) Four elliptical vias to create single capture well and Solid Penetrator later; (b) Lower magnification view of a portion of the elliptical vias array.

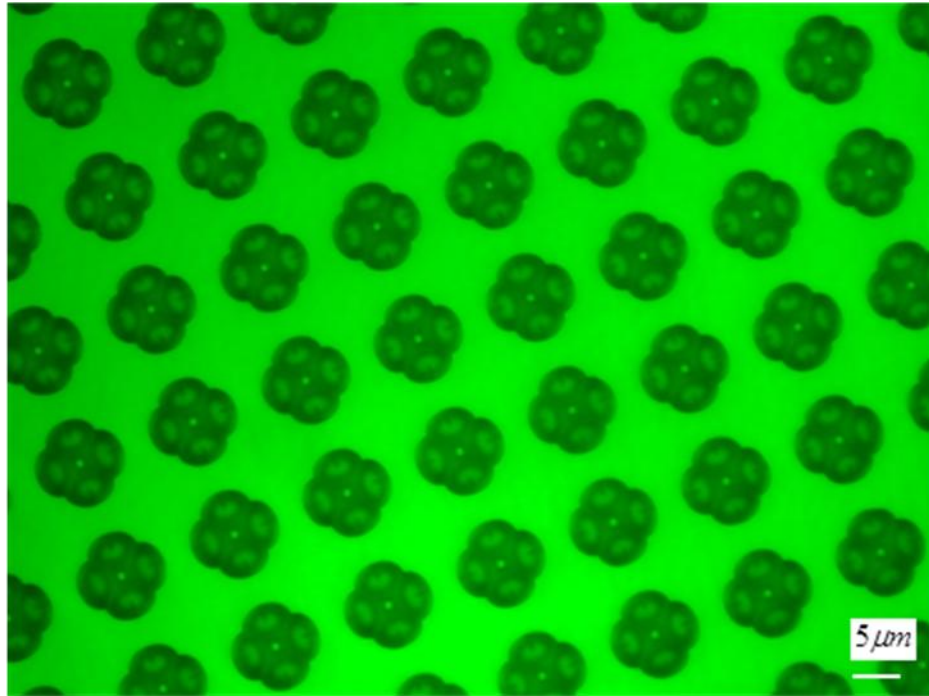
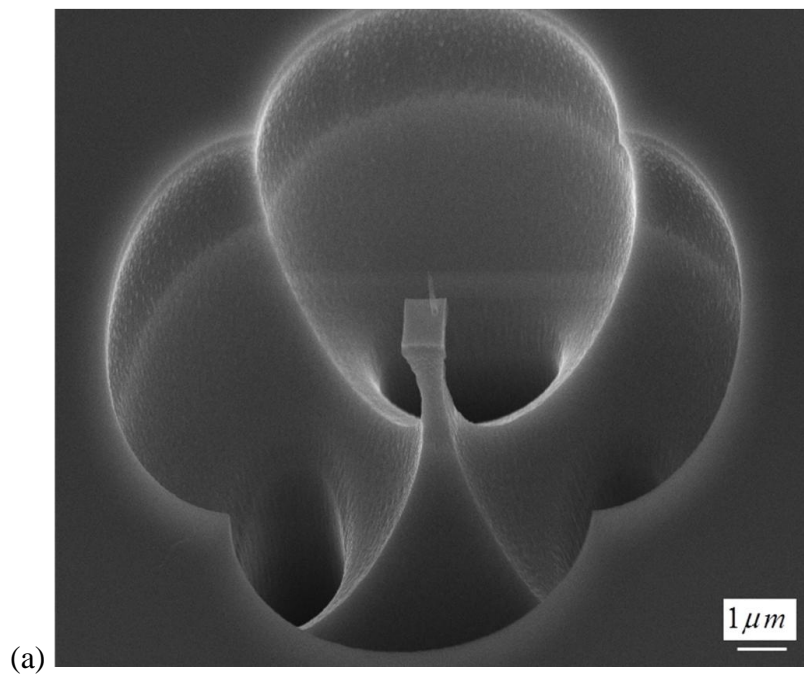


Figure 3.3 Optical microscope image of a portion of the 100 by 100 capture site array after isotropic etching.



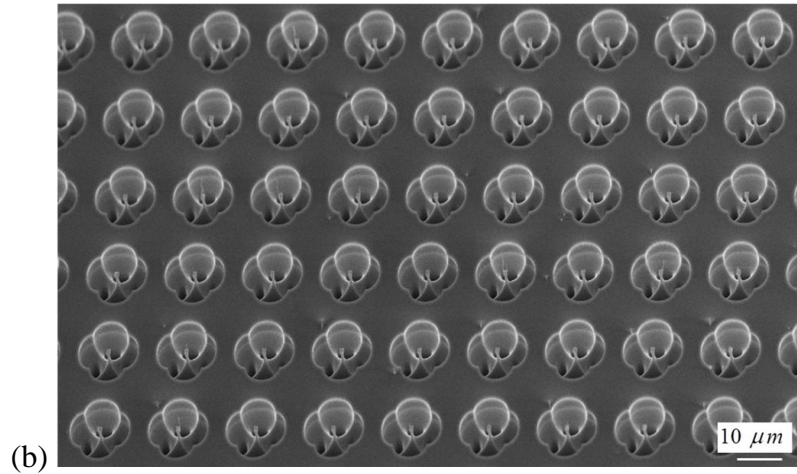


Figure 3.4 SEM images of capture wells and Solid Penetrators after isotropic etching and via anisotropic etching. (a) Single capture well monolithically integrated with Solid Penetrator; (b) Lower magnification of a portion of the 100 x 100 capture site array.

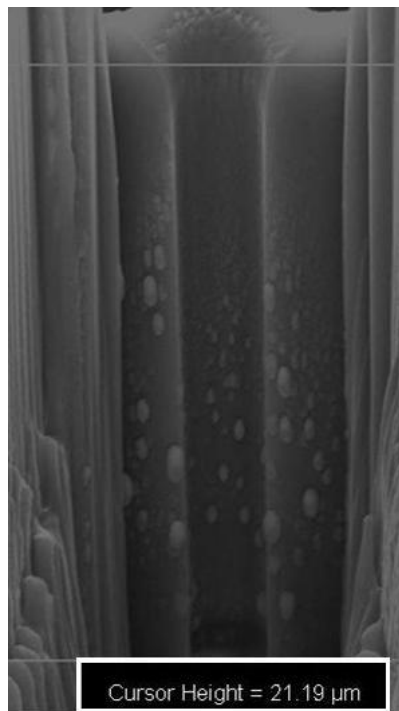


Figure 3.5 SEM image of Focused Ion Beam Milled single via's cross section.

In step 4, Cl₂ anisotropic etching (Panasonic ICP Etcher E 620-R&D, UCSB) refines the Solid Penetrator tips to be about 0.5 μm or less, while the bases of the Solid Penetrators are about 2 μm in diameter. A following CF₄ / O₂ dry etching (STS Multiplex RIE, UCR) takes off Cl₂ etching passivation film around Solid Penetrators and on Capture Site side walls.

The following is the detailed process flow outlining the microfabrication procedures of step 4:

(1) Silicon Cl₂ anisotropic etching- solid penetrator refinement

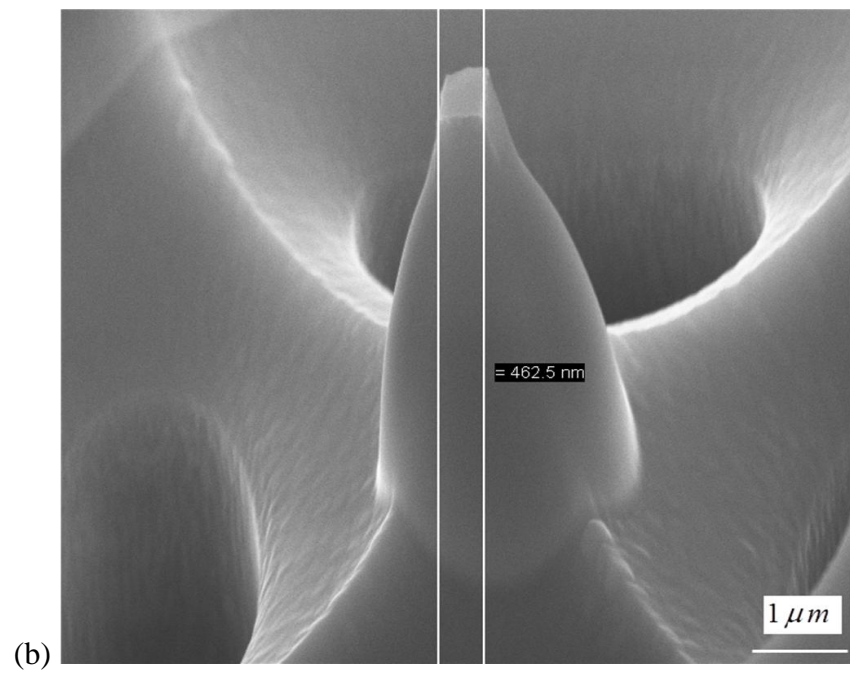
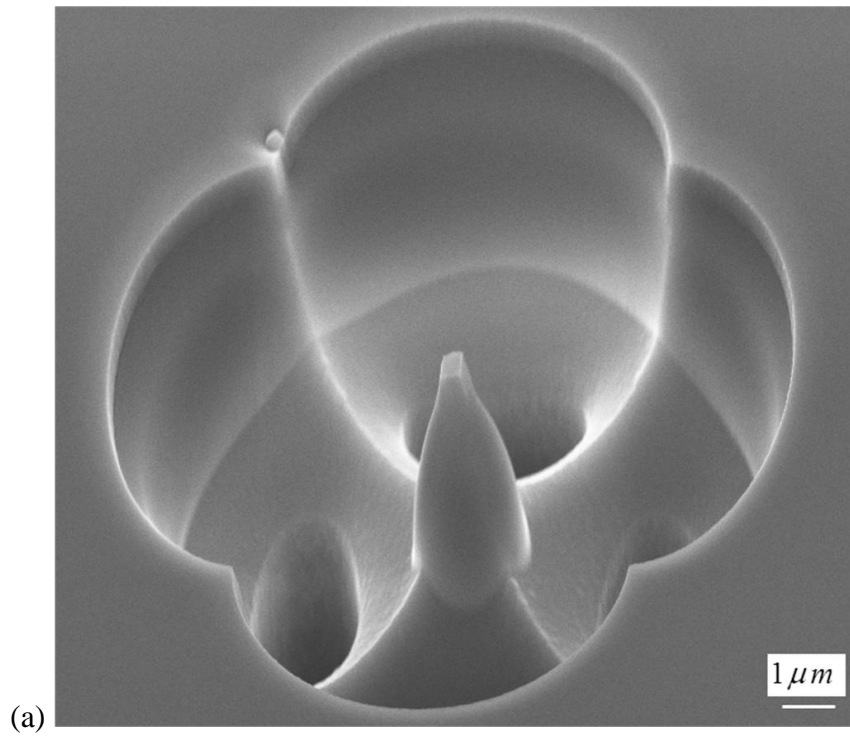
- 400 W ICP source power, 12 W sample RF power, 1.2 Pa pressure, 10 sccm Cl₂
- ~ 5 min etch

(2) Verification of capture wells and Solid Penetrator feature size and uniformity using SEM (Leo SUPRA 55 system, UCR), as shown in Figure 3.6.

(3) Chlorine passivation removal dry etching

- 300 W Power, 100 mTorr pressure, 40 sccm O₂ and 50 sccm CF₄
- Etch time depends on size measurement from (2), e.g. Figure 3.5 (b) (c).

(4) Verification of capture wells and Solid Penetrator feature size and uniformity using SEM (Leo SUPRA 55 system, UCR), as shown in Figure 3.7.



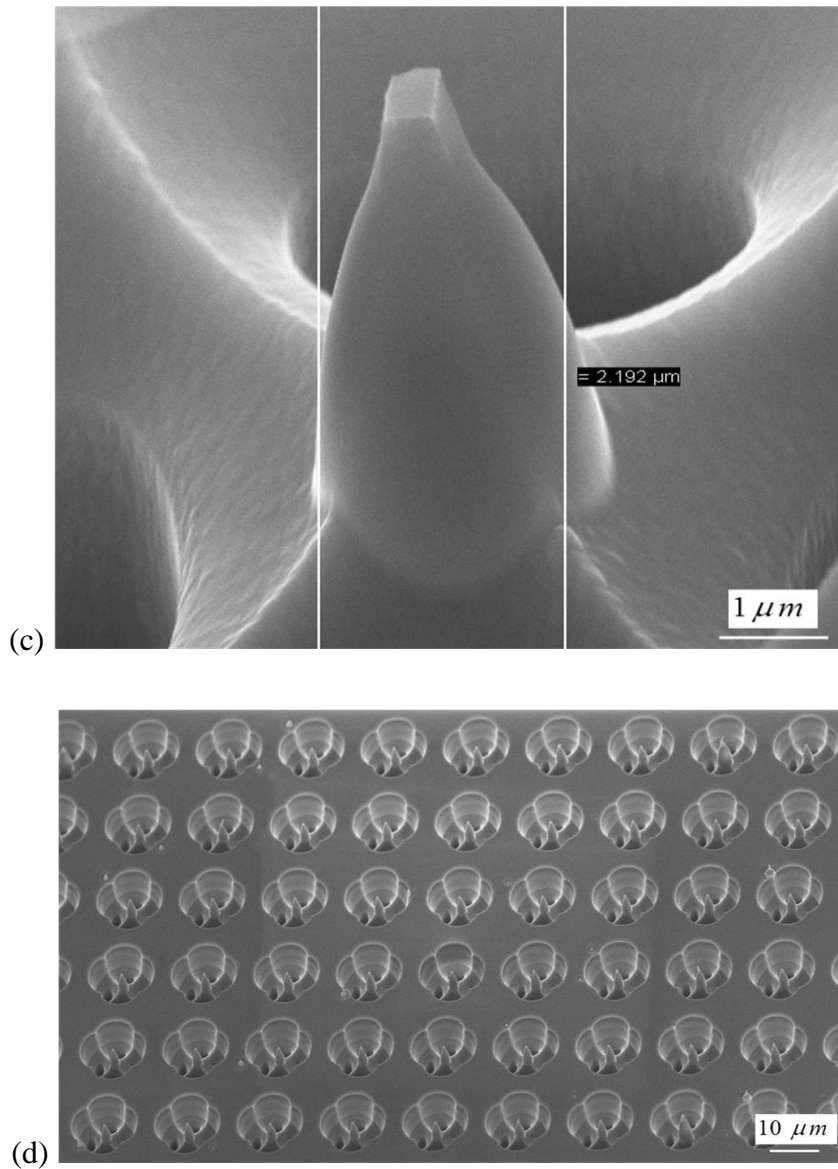
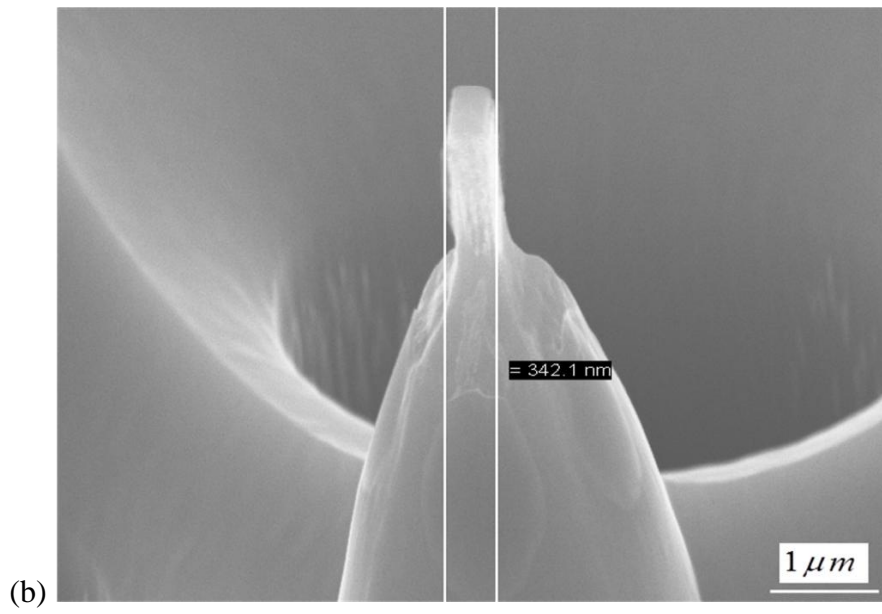
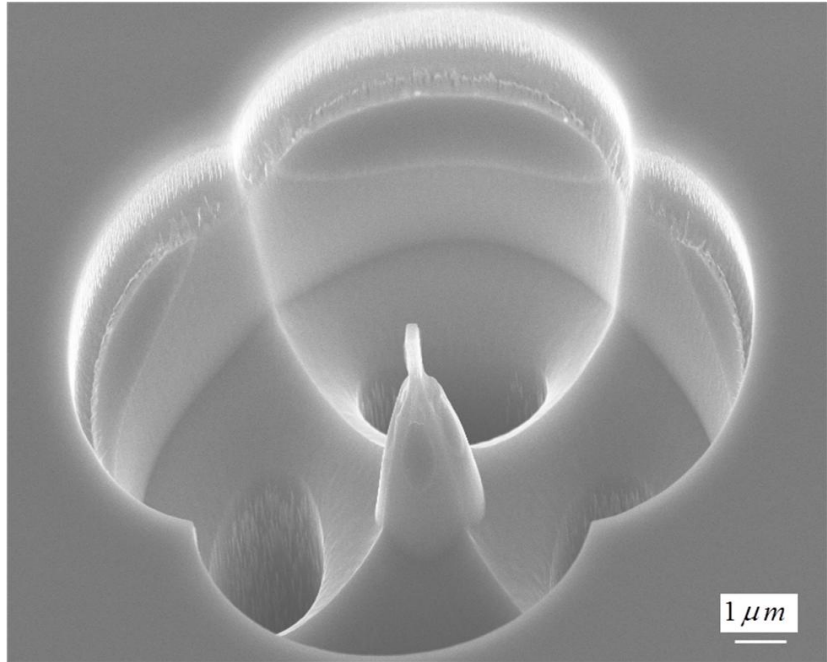


Figure 3.6 SEM images of capture wells and solid penetrators after Cl_2 etching. (a) Single capture well monolithically integrated with Solid Penetrator; (b) Higher magnification view and measurement of the single Solid Penetrator top; (c) Higher magnification view and measurement of the single Solid Penetrator passivation wildest part; (d) Lower magnification of a portion of the 100×100 capture site array.



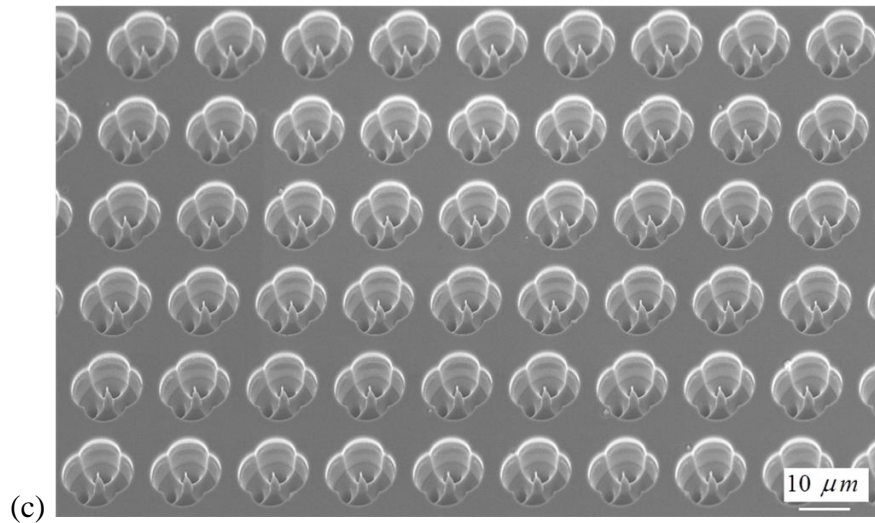


Figure 3.7 SEM images of capture wells and Solid Penetrators after Chlorine passivation removal dry etching. (a) Single capture well monolithically integrated with Solid Penetrator; (b) Higher magnification view of the single Solid Penetrator, with about 342nm by 928 nm sharp top; (c) Lower magnification of a portion of the 100 x 100 capture site array.

In step 5, SiO₂ mask layer on handle layer and BOX layer exposed to patterns are removed by CF₄/ CHF₃ dry etching (STS Multiplex RIE, UCR), as shown in Figure 3.8. Piranha cleaning and O₂ ashing (UCR) afterward get rid of organic residuals and particles from the SiO₂ mask removal step.

(1) SiO₂ mask and BOX layer removal dry etching- handle layer and BOX layer

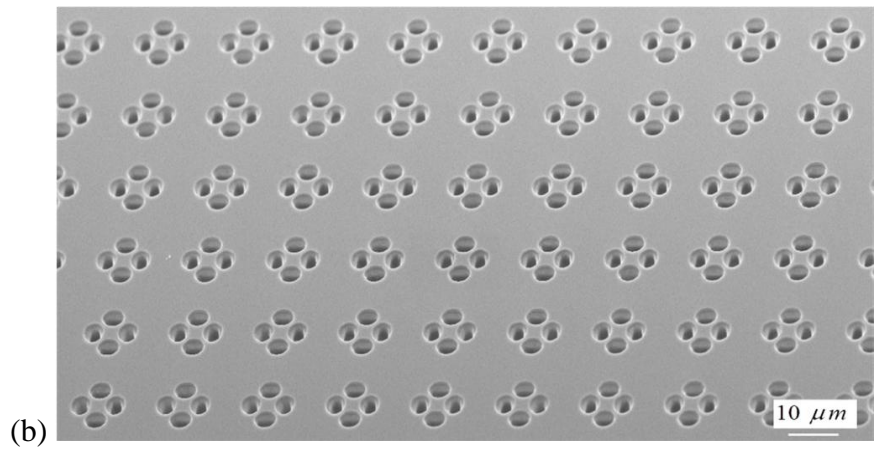
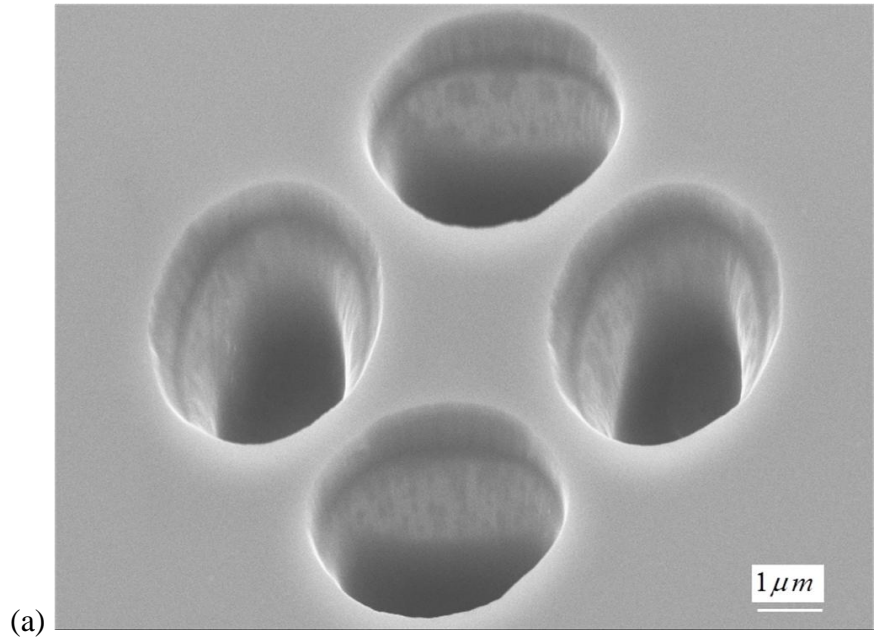
- 300 W power, 100 mTorr, 30 sccm CHF₃, 20 sccm CF₄
- ~ 14 min etch

(2) Clean samples

- Piranha: mixture of H_2SO_4 (96% concentration) and H_2O_2 (30% concentration), ratio 1:1, 30 min
- O_2 ashing: 0.6 mbar, 100 W power, 5 mins

(3) Verification of aspiration vias and aspiration port feature size and uniformity using SEM (Leo SUPRA 55 system, UCR), as shown in Figure 3.8.

The 4 inch SOI wafer can produce 21 device chips, which is cut into 21 pieces before step 3. And all the process parameters listed above after step 2 are for single piece of device chip fabrication. Theoretically, those parameters will have slight change if fabricating multiple pieces of device chip together, especially for dry plasma etching (Bosch / ICP / RIE). However, currently up to 7 pieces of device chip can be managed to be etched in the same batch with the same parameter as for single piece fabrication, without obvious influence on patterned features. We indeed noticed that there are slight differences among each of those pieces after isotropic etching in step 3, depending on certain position that each piece sitting on carrier wafer, i.e. in the etching chamber. But those variances are acceptable. We are trying to handle fabrication with more pieces of device chip in a same batch, to achieve batch fabrication with full 4 inch wafers in the future, which can reduce fabrication time per device significantly.



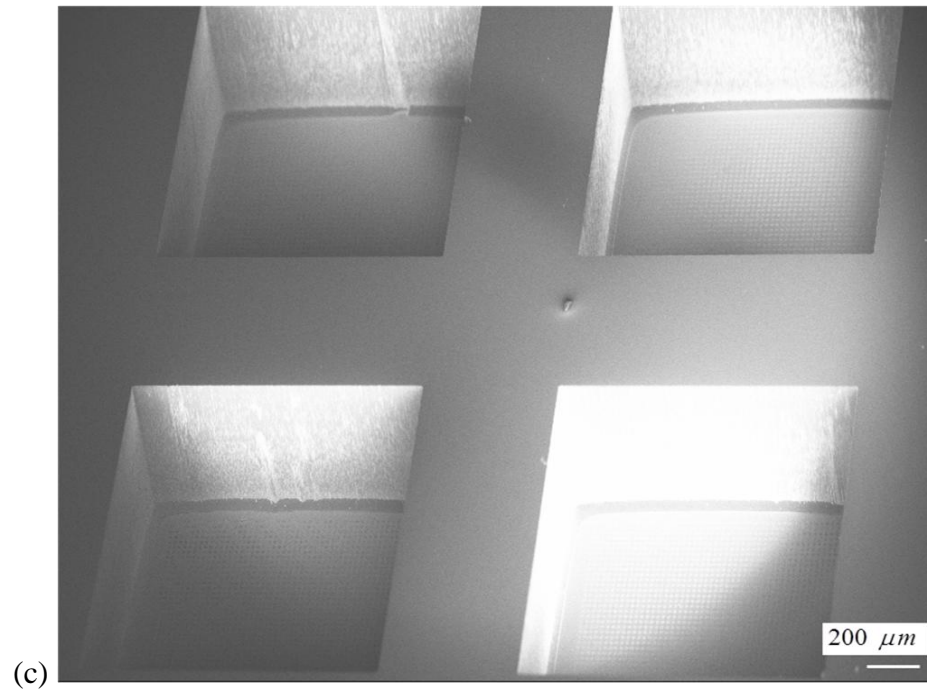


Figure 3.8 SEM images of handle layer of device chip. (a) Four vias within single capture site connecting with big Aspiration port; (b) Lower magnification view of a portion of the 100 x 100 vias array; (c) View of aspiration big ports on handle layer of substrate.

4. Device characterization

4.1 Preliminary functional verification

Before cell capture, permeabilization and transfection functions' test of the device chip, preliminary device functional verification tests were carried out, including fixture set construction, flow circuit development, leaking elimination and pressure range validation.

4.1.1 Fixture set construction

A fixture set was designed and fabricated to support the device chip, as well as provide channels to connect the device chip and external tubing to build the functional flow circuit, as shown in Figure 4.1. The bottom part of the fixture set is connected with external tubing through the side wall hole, while the tubing is connected with a syringe on syringe pump, providing bi-directional aspiration flow. The top part of the fixture set

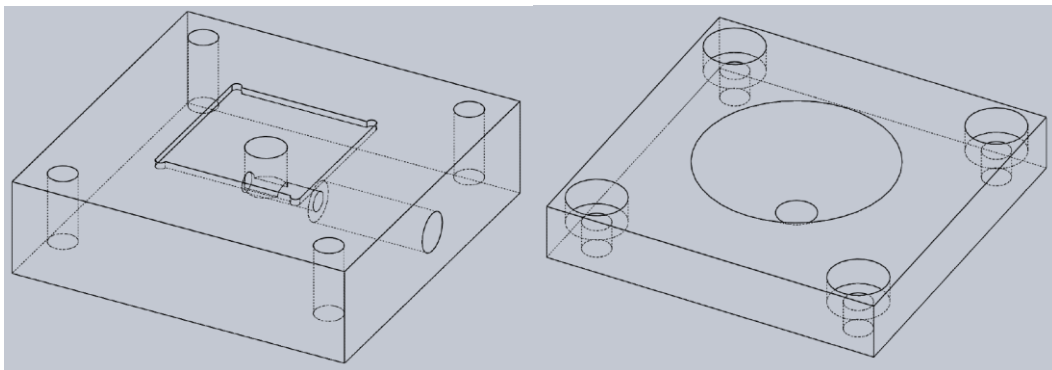


Figure 4.1 Schematic of the fixture set. (Left): bottom part of the fixture set, holding device chip in the middle reservoir. (Right): top part of the fixture set.

has a 650 μL reservoir to hold test liquid, which can be sucked onto the device chip underneath directly. The bottom and top parts can clamp the device chip in the middle, and are assembled together by four screws on corners. The fixture set parts are designed and then produced by Computer numerically controlled (CNC) machining (Firstcut, Proto Labs) using polycarbonate.

4.1.2 Flow circuit development

In the flow circuit, a syringe pump (Harvard Apparatus PHD ULTRA) was used to provide bi-directional constant flow rate flow as aspiration flow, whose syringe is connected with the fixture set using tubing and adaptors (IDEX Health & Science), which are biocompatible and good to use for high-pressure applications. A pressure transducer (Omega DPG 4000-15) was T-off into the main line of the circuit to detect pressure changes.

4.1.3 Leaking elimination

Test liquid (DI water here) was observed leaking between the device chip and both the bottom / top parts of the fixture set. To seal the gaps, a commercial PDMS film sheet (McMaster-Carr) with 0.125 mm thickness was utilized. After being cutted into the device-chip- size pieces, and cutted a hole in the middle which is a little bit larger than the Solid Penetrator arrays, the PDMS film pieces are temporarily bonded on both sides of the device chip as gaskets. After operation, temporarily bonded PDMS gaskets can be peeled off easily and cleaned by Acetone / Isoproponal / DI water rinse. The PDMS gaskets efficiently eliminate leaking.

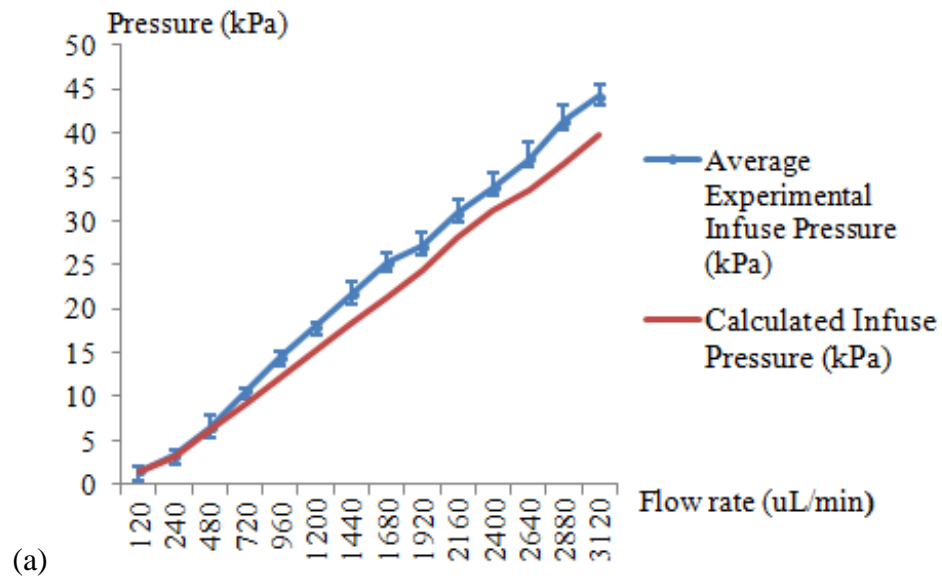
4.1.4 Pressure validation

Utilizing the flow circuit developed, several preliminary functional tests increasing flow rate from 120 $\mu\text{L}/\text{min}$ to 3120 $\mu\text{L}/\text{min}$ for both infuse / withdraw flow were carried out. Corresponding pressure readings for each flow rate were recorded, and compared with analytical calculated results, as shown in Figure 4.2. Both tested infuse and withdraw pressures change in reasonable trend that agrees with analytical calculation results, while 6.72% normal root mean square deviation (NRMSD) of infuse pressure and 5.83 % NRMSD of withdraw pressure are observed. Those deviations could be resulted from minor clogging caused by unfiltered DI water in the device chip, which are acceptable.

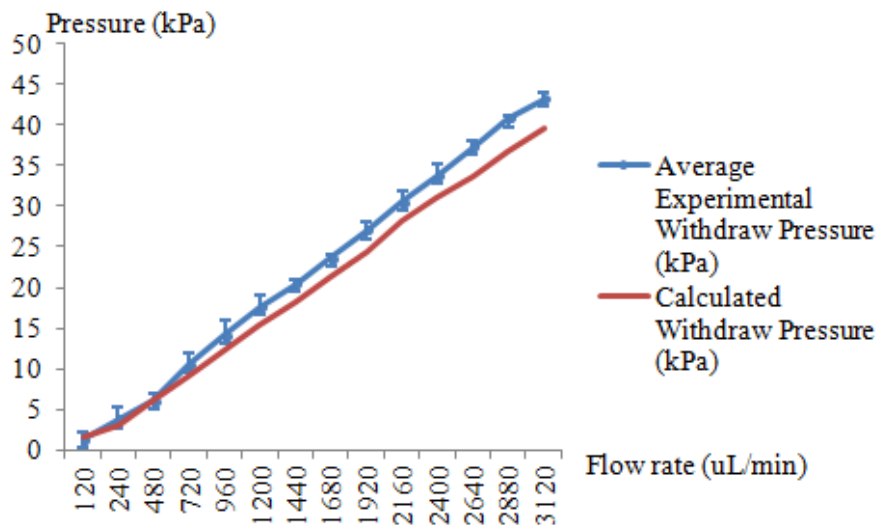
From the pressure validation test, the device chip membrane robustness was also verified, which is intact after being executed up to about 45 kPa pressure with up to about 3 mm / min flow rate, while the maximum operation flow rate will be only about 270 $\mu\text{L}/\text{min}$ with about 1.37 kPa as estimated from Chapter 2. Therefore, the device chip and the whole flow circuit are ready to be used in cell tests.

4.2 Cell tests

The cell tests are performed by Professor Ballas' lab in Division of Hematology/Oncology, Indiana University School of Medicine, and in Professor Rao's and Tsutsui's labs, University of California-Riverside. Professor Ballas' lab manipulates non-adherent K562 cells while Professor Tsutsui's and Rao's labs utilize adherent MEF cells.



(a)



(b)

Figure 4.2 (a) Comparison between measured infusion pressure readings from several tests and analytical calculation results. (b) Comparison between measured withdraw pressure readings from several tests and analytical calculation results. Plotted measurements are averaged values at each flow rate for 3 separate tests. Error bars represent standard deviation.

4.2.1 K562 Cell tests

In most K562 cell studies, test samples were prepared in a single device operation cycle by: 1) pipetting 50k cells per 20 μL buffer onto the fixture set reservoir; 2) capturing cells via negative aspiration flow at flow rate 10 $\mu\text{L}/\text{min}$ for 30 sec; 3) washing excess uncaptured cells with pipetting; 4) penetrating captured cells using slightly greater negative aspiration flow at flow rate 70 $\mu\text{L}/\text{min}$ for 5 sec; 5) releasing penetrated cells using positive aspiration flow at flow rate 1 mL/min for 5 sec; and 6) collecting released cells by pipetting. At least 1 such cycle was performed in each experiment, with up to 3 cycles completed in some experiments. Cell counting utilized manual hemacytometric and automated flow cytometric approaches. Addition of vital dye to the collected cell suspensions enabled quantification of penetration (trypan blue and propidium iodide, for hemacytometric and flow cytometric counting, respectively).

Table 4.1 Penetration efficiency of K562 cells from manual hemacytometric counting.

Samples	Cycles		% Dye Positive
Background	N/A		9.8
Negative Control	N/A		10.8
Positive Control	N/A		99.9
Test 1	2, combined	cycle 1+2	62.7
Test 2	2, separate	cycle 1	57.1
		cycle 2	18.1

Also prepared were samples for: 1) *Background* - cells collected, centrifuged, and vortexed; 2) *Negative Control* - cells pipetted onto device surface, held quiescent for 1

min, collected, and then processed similarly to test samples; and 3) *Positive Control* - similar to *Background* samples, but with addition of detergent NP40 to disrupt the cell membrane.

Results from hemacytometric counting are shown in Table 4.1 and indicate cell

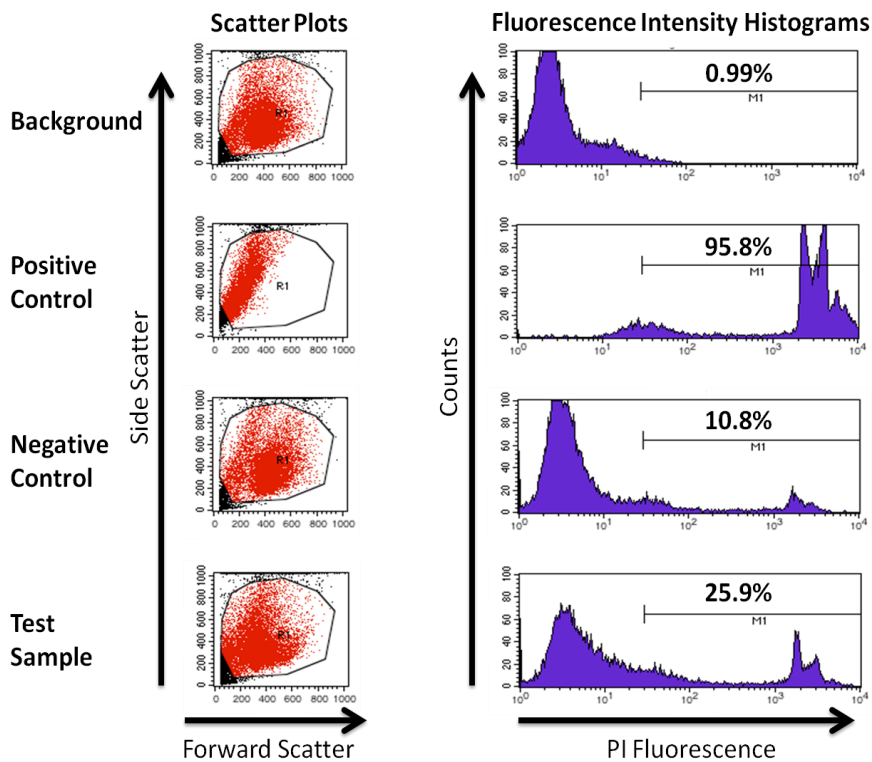


Figure 4.3 Flow cytometry results for UHT mechanoporation device: (Left) Scatter plots (cell size/granularity) showing non-porated cells occupying larger population in center of plots and porated cells occupying population near side scatter axis; (Right) Histograms of cells pooled from 15 operation cycles showing overall poration efficiency of ~15% (percent dye positive cells indicated on each plot).

penetration efficiencies up to 50% greater than the *Background* and *Negative Control* for single cycle experiments. However, results from multiple cycle experiments indicate that efficiency can decrease in such situations. Results from flow cytometric counting are shown in Figure 4.3 and indicate lower overall penetration efficiency, which is ~ 15% (above negative control).

The overall low cell penetration efficiency could result from several key issues. First, cell debris from previous runs can cause aspiration vias clogged, thus insufficient device chip cleaning will result in lower and lower subsequent tests' efficiencies, especially when multiple tests utilized the same device chip. This could also explain the higher penetration efficiency from the first single cycle operation but lower penetration efficiency from the subsequent cycles as shown in Table 4.1. Second, without rigorous flow circuit flushing, bubbles could be trapped underneath the device chip and block quite amount of aspiration via arrays to be usable. Finally, the operation parameters (i.e. capturing / puncturing / releasing flow rate and time) are set based on previous cell manipulation experience, which could likely be further optimized to improve efficiency.

4.2.2 Fluorescent beads tests

To identify the above issues' influence on the device chip performance, more tests were carried out in Professor Rao's and Tsutsui's lab. Firstly, the system was characterized using polystyrene fluorescent beads (15.5 μm -mean diameter, P(S/2%DVB) · (480,520), Bangs Laboratories). The entire setting is shown in Figure 4.4. In the tests, 70k beads in 20 μL PBS solution were pipetted onto the fixture set reservoir.

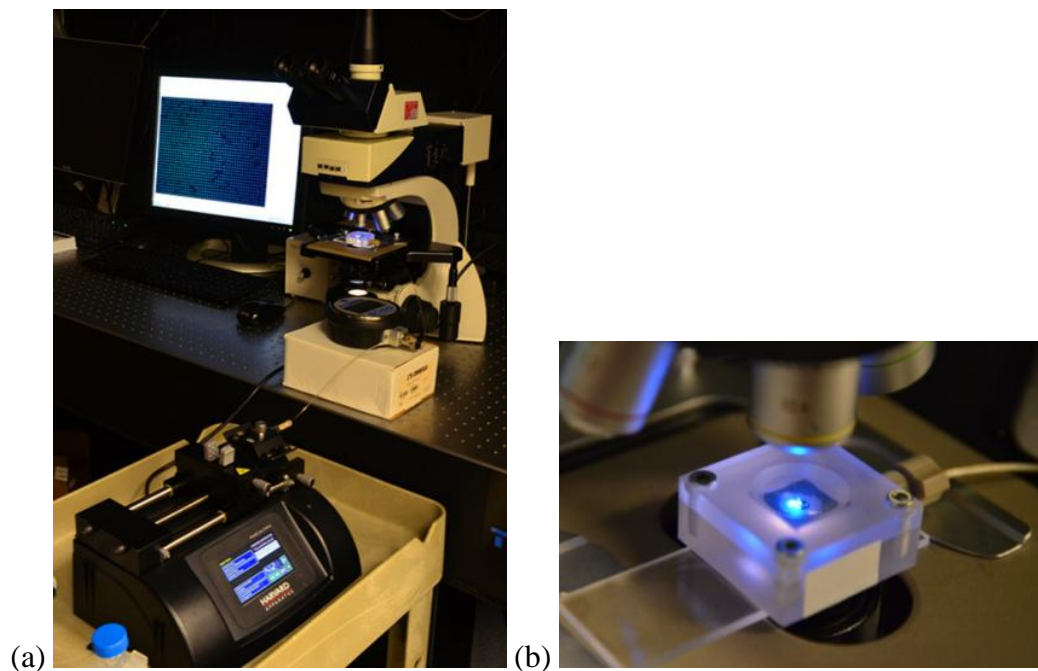


Figure 4.4 Images of UHT mechanoporation device chip test setting: (a) Entire setting including syringe pump, pressure meter, fixture set with device chip, and microscope; (b) Fixture set with device chip sitting under microscope.

In the first several trials, it is observed that beads populated unevenly into the capture well arrays. After combining microscope bottom light source, we found out that bubbles were indeed trapped underneath certain capture well arrays and caused this non uniform distribution, as shown in Figure 4.5 (a). With completely flow circuit flushing before adding beads (or cells in the following tests), bubbles can be eliminated thus device chip is well functioned, as shown in Figure 4.5 (b).

Since fluorescent beads are rigid solid particles, puncturing is impossible to realize. Hence only capturing flow rate and time were varied to improve population

efficiency. During beads capturing, negative aspiration flow was stopped before obvious aggregation but not 30 sec as in K562 cell tests. Washing excess uncaptured and aggregated beads during capturing helped to get better distribution. Different capturing flow rates were applied, i.e. 10 / 20 / 40 $\mu\text{L}/\text{min}$, as shown in Figure 4.6. Population efficiency is significantly increased from about 9.6% at flow rate 10 $\mu\text{L}/\text{min}$ for 2 min, to about 75.2% at flow rate 40 $\mu\text{L}/\text{min}$ for 1 min. It demonstrates that population efficiency can be prominently improved by optimizing capturing flow rate / time for fluorescent beads.

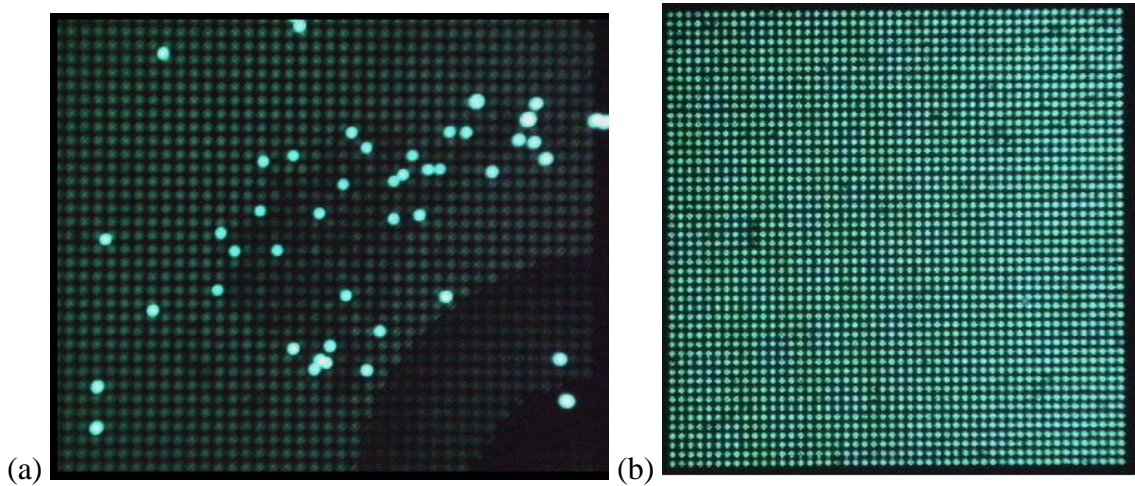


Figure 4.5 Fluorescence images of: (a) bubbles being trapped underneath capture well arrays and (b) bubbles being completely eliminated from capture well arrays after rigorous flushing.

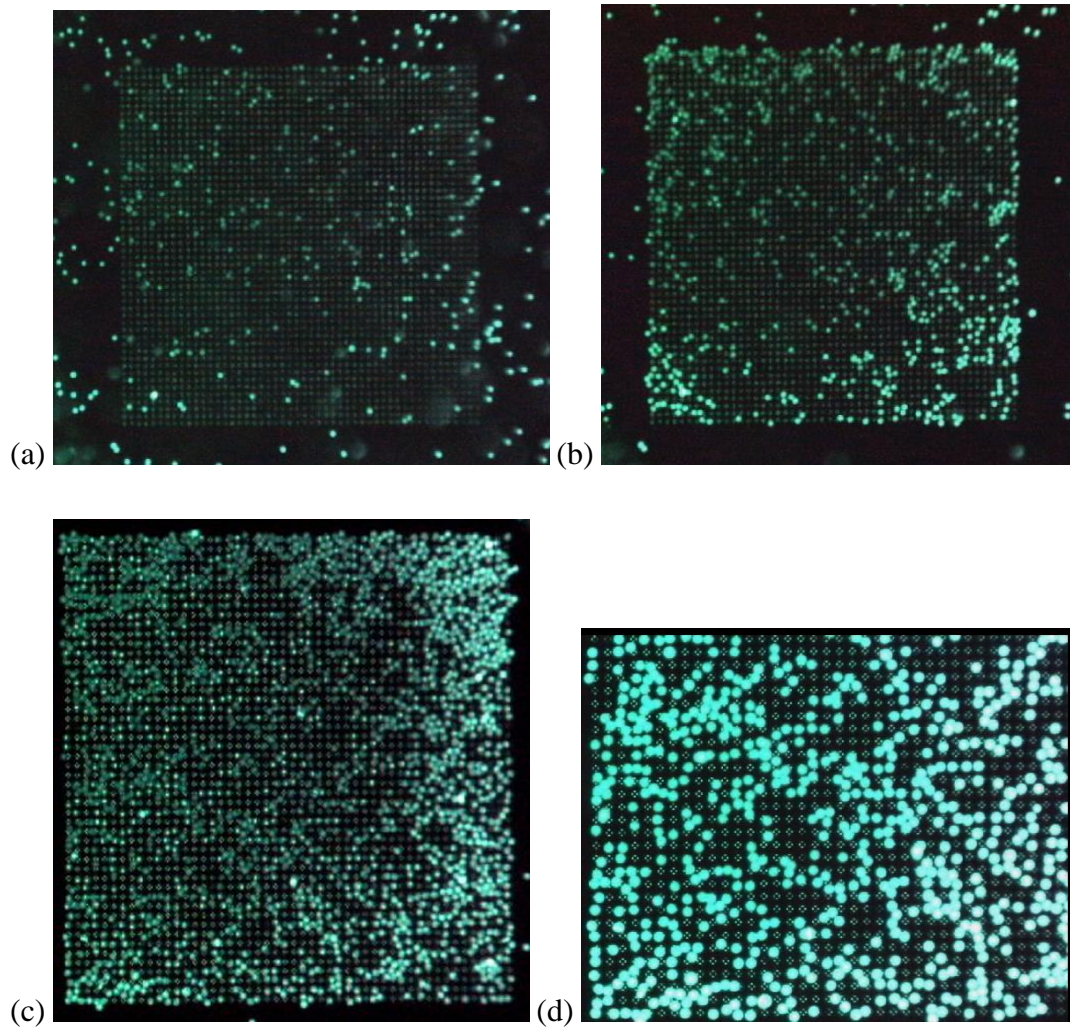


Figure 4.6 Fluorescence images of polystyrene beads' population on device chip with different flow rate and time: (a) bead's population (about 9.6%) with flow rate $10 \mu\text{L}/\text{min}$ for 2 min; (b) bead's population (about 20%) with flow rate $20 \mu\text{L}/\text{min}$ for 2 min; (c) bead's population (about 75.2%) with flow rate $40 \mu\text{L}/\text{min}$ for 2 min; (d) Higher magnification of lined up beads with flow rate $40 \mu\text{L}/\text{min}$.

4.2.3 MEF cell tests

Other than fluorescent beads, MEF cells were utilized with live / dead sustain for more studies, which is easier to prepare and operate than K562 cells. In this study, cell samples were prepared in a similar device operation cycle as for K562 cells. The differences are that, we stopped capturing and puncturing cells in steps 2 and 4, respectively, when no more significant changes of capturing / puncturing cell population

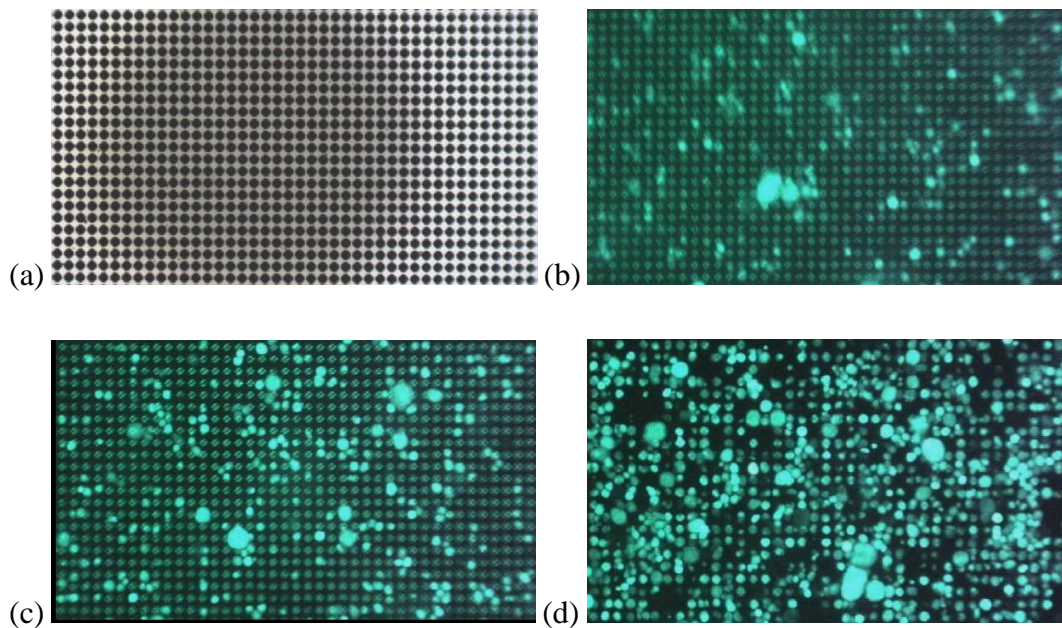


Figure 4.7 Fluorescence images of MEF cells population at a fixed position in the capture site array during an operation cycle: (a) Cell capturing started at flow rate $10 \mu\text{L}/\text{min}$; (b) Washing away excess uncaptured cells with pipette at 60 sec while capturing aspiration pressure is still provided; (c) Stop cell capturing at 110 sec and change pump flow rate to $70 \mu\text{L}/\text{min}$; Cell puncture started at 125 sec at flow rate $70 \mu\text{L}/\text{min}$; (d) Stop cell puncturing at 165 sec.

on capture wells were observed. Thus, the capturing step took 110 sec rather than 30 sec for K562 cells, while puncturing step took 40 sec rather than 5 sec for K562 cells. Fluorescent images of MEF cells population on capture wells at different time spots are shown in Figure 4.7. Corresponding pressure drop plot from pressure transducer recording is shown in Figure 4.8.

Right before washing excess uncaptured cells, about 18% of capture wells have been populated with live cells, as shown in Figure 4.7 (b) (The portion of capture wells shown in Figure 4.7 is a 23 x 41 array, totalling 943 capture wells). When cell capturing stopped, about 25% of capture wells have been populated with live cells in the same area, as shown in Figure 4.7 (c). At last, after ceasing cell puncturing, about 75% of capture wells have been populated with live cells, as shown in Figure 4.7 (d). On the other hand, cell population at 30 sec during capturing is about 8%, while the first 5 sec puncturing caught about only 2% more cells (data not shown). It demonstrates that cell penetration efficiency could be significantly improved by operation parameter optimization.

Figure 4.8 exhibits pressure drop in the MEF cell study as well as in a control study with cell buffers but without cells. In the MEF cell study, the pressure drop achieved the stable value after about 20 sec during cell capturing, which is the same as in the control study. It suggests that while cells are drawn to the capture sites (as evidenced by the increasing cell population in Figure 4.7), the flow rate is insufficient to draw the cells within the capture wells themselves (as evidenced by the minimal change in pressure drop). After cell puncturing beginning, the pressure drop kept increasing to a two-fold greater value than the stable value in the control study when the puncturing

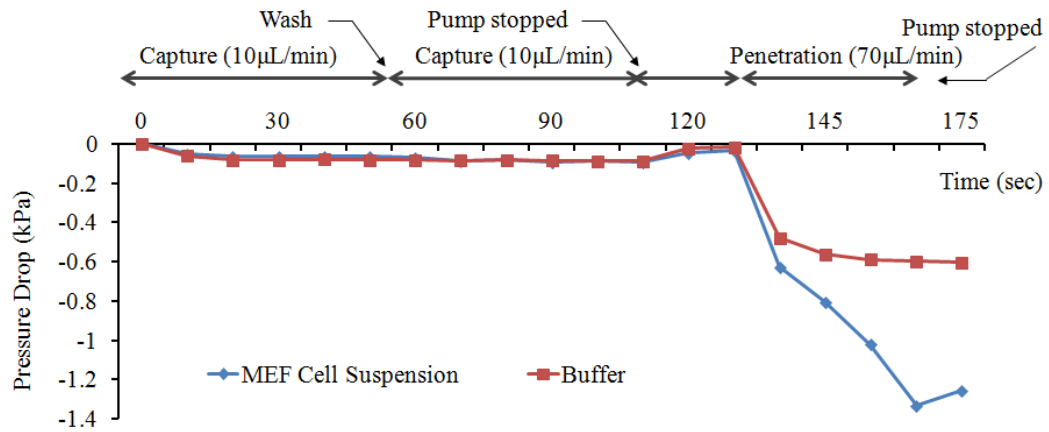


Figure 4.8 Pressure change plot from pressure transducer recording during the MEF cell study and a control study.

stopped. The increase within the first 10 sec could result from the pump ramp since it also took about 10 sec for the pressure drop to achieve the stable value in control study. However, as more and more cells being captured and punctured onto the Solid Penetrators, capture wells as well as aspiration vias were gradually populated and filled. Thus, the continual pressure increase in MEF cell study in the following 30 sec may have been due to flow rate increase through the remaining unpopulated capture sites to meet the constant flow rate condition imposed on the aspiration circuit. Consequently, as pressure on the captured cells increases, the potential for cell lysis increases, thus reducing poration efficiency. Hence we hypothesize that efficiency will also be improved in the near-future through implementation of pressure-based control for the aspiration circuit, rather than the current flow rate control approach.

5. Future Directions

To achieve the final application goal of the UHT device, i.e. ex vivo cell therapy, there are several key processes needed in the future to consummate the full functions of the device and its affiliated system. The future effort will enable active injection function and automated transportation function of the device and entire system, which will be able to minimize necessary human interaction and achieve ultrahigh throughput to generate clinically-relevant numbers of cells.

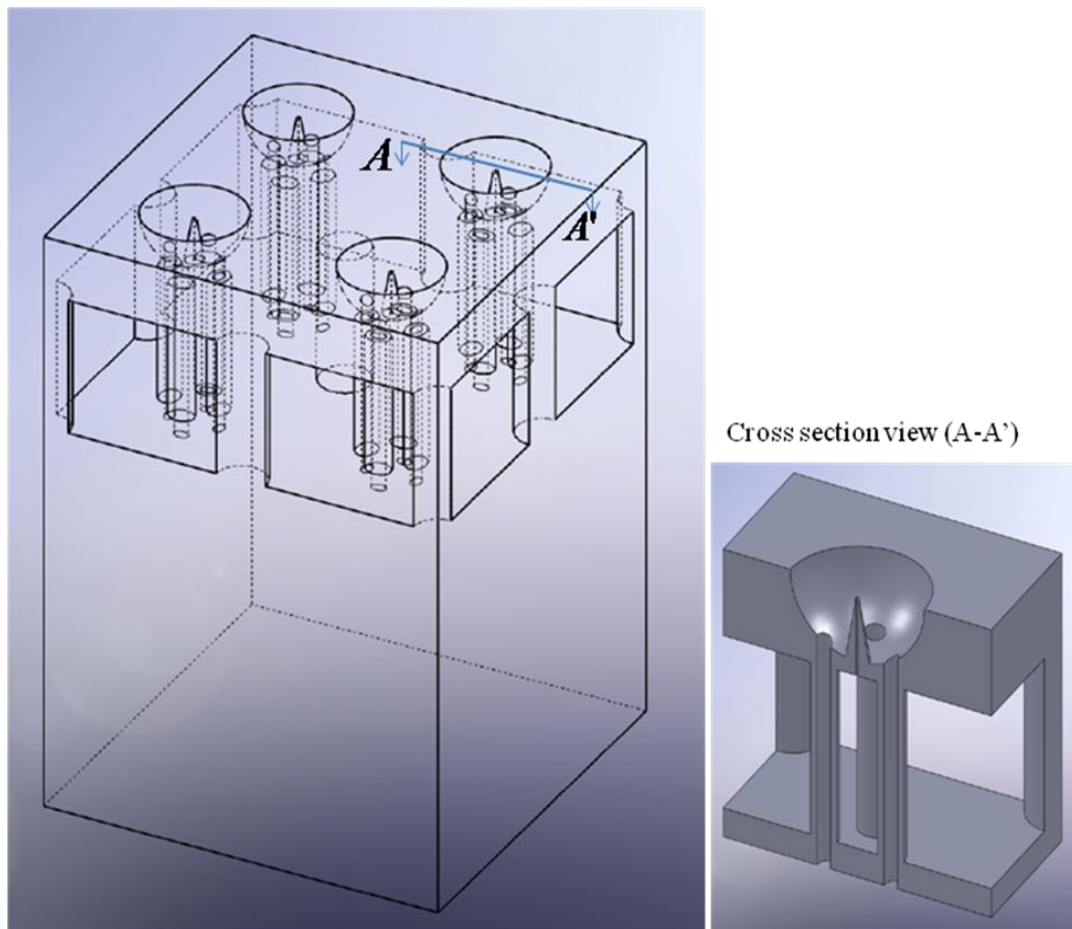


Figure 5.1 Schematic of a portion of the UHT active microinjection device.

To enable active injection function, Solid Penetrators are going to be replaced by hollow needles, and injection circuit will be introduced into device chip, as shown in Figure 5.1. To enable automated transportation function, flow inlet / outlet ports will be added on the device chip, so that affiliated parts can transport cell suspension towards the microneedle arrays as well as collect the manipulated cells. The affiliated parts and active microinjection device chip are shown in Figure 5.2. The Cover Plate with Flow Channel that directs cells to the capture array and then away for collection will be manufactured

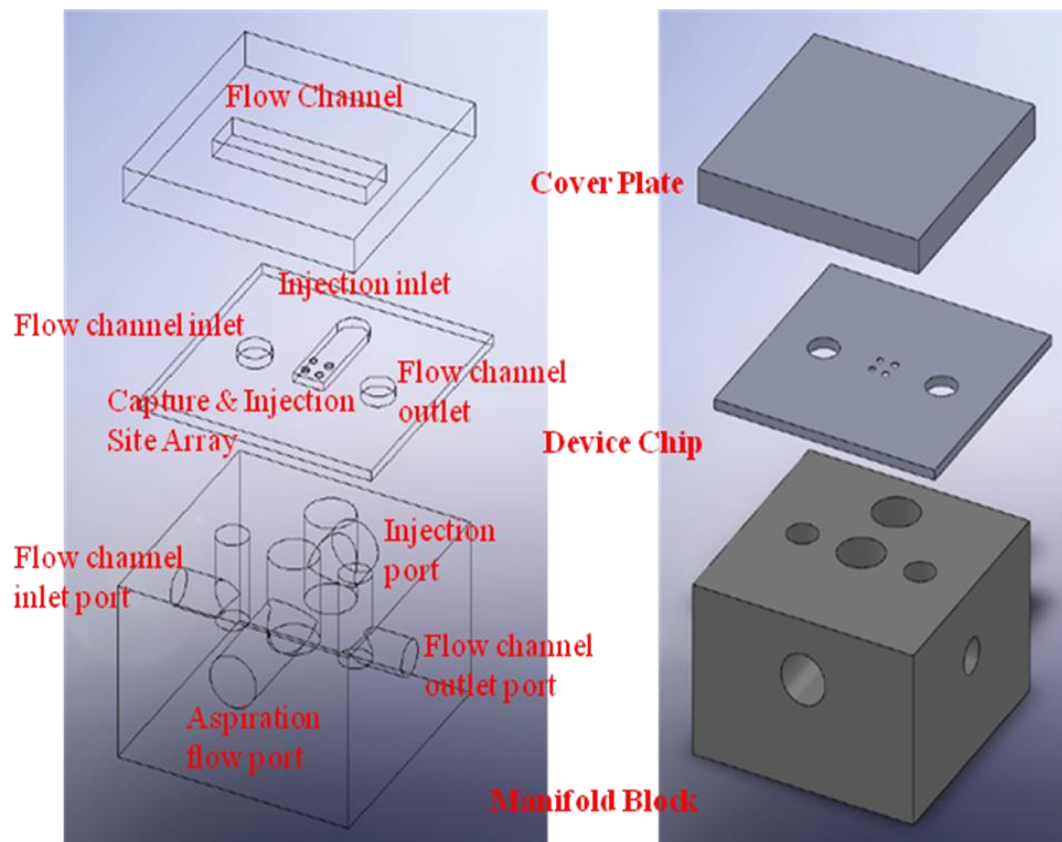


Figure 5.2 Schematics of the UHT active microinjection device and affiliated parts.

with PDMS. The Manifold Block that connects the Aspiration, Flow Channel and Injection ports with external syringe pumps will be fabricated with acrylic.

5.1 UHT active microinjection device chip fabrication

To fabricate the UHT active microinjection device, the established microfabrication process in Chapter 3 needs additional steps to build the injection circuit, as shown in Figure 5.3. Two 100 mm - diameter SOI substrates will be used, first of which will provide the thin Si layer in which the Capture Sites will be defined as in current completed devices, and the second substrate will contain the underlying fluidic circuits and backside ports.

The second substrate will be a wafer with 14 μm Si device layer, 2 μm BOX layer, and 500 μm Si handle layer. The device layer of the second substrate will be coated with a 1 μm SiO₂ etching mask using thermal oxidation and patterned with the Aspiration Via Columns with projection lithography. After transferring those patterns into the SiO₂ mask using RIE dry etching, the Injection Inlet and Flow Channel Inlet/Outlet ports will be aligned-patterned with contact-lithography. These will be transferred to the SiO₂ etching mask using RIE dry etching, too. Before removing the photoresist mask, the Injection Inlet and Flow channel Inlet/Outlet ports will be etched 5 μm via Si DRIE. Then the photoresist mask will be removed and the device layer will be etched another 9 μm using Si DRIE till extended to the BOX layer. The SiO₂ mask will then be removed with RIE dry etching. Finally, the aspiration / Flow Channel Inlet / Outlet ports on substrate handle layer will be etched by DIRE Bosch process as in current

device and extended to BOX layer. In the end, the BOX layer exposed to ports will be dry etched using RIE. All the processes will be performed using the same tools as in the current device fabrication.

The handle layer of the first substrate will be removed using wet etching in advance. The newly exposed BOX layer will then serve as an etching mask for the

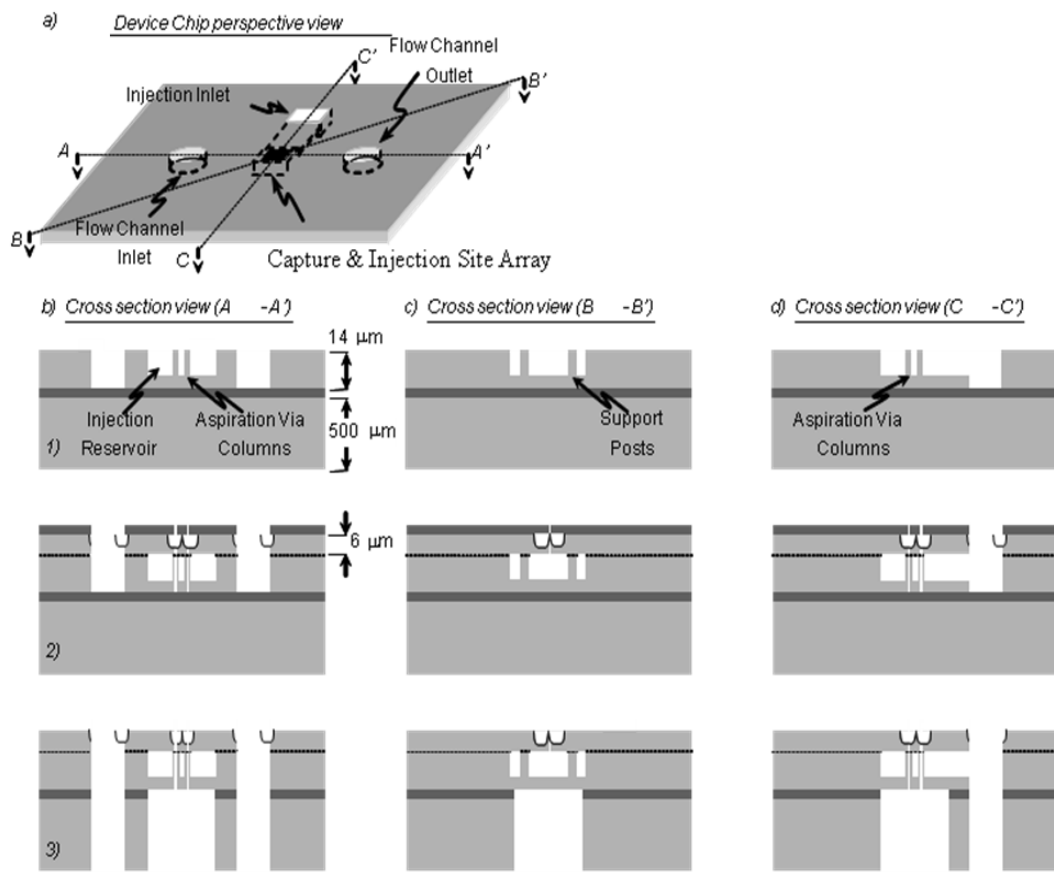


Figure 5.3 Abridged microfabrication process flow for UHT active microinjection device. Dotted line indicates the bonded interface. Only one unit cell site is shown for the sake of clarity.

definition of the Capture Sites and Injection needles. The aspiration vias and injection lumens will be projection lithographically patterned and transferred into the BOX layer using RIE dry etching. Then the Injection and Flow Channel Inlet/Outlet ports will be patterned using contact-lithography and transferred into the BOX layer with RIE dry etching. Additionally, another contact-lithography will pattern protection dots covering injection lumens as protection from isotropic etching. After isotropic etching to define the Capture Sites and Solid Penetrators, Si DRIE will etch through the Injection and Flow Channel Inlet/Outlet ports, as well as the aspiration vias and injection lumens. Finally, the BOX layer will be etched with RIE dry etching.

Then the second substrate will be bonded face to face with the first substrate. Due to insufficient resolution, direct verification of bond quality using non-destructive inspection is not possible, thus quality will be verified by device performance in cell manipulation.

5.2 Affiliated system development

The acrylic manifold block can be obtained from Firstcut. And the cover plate can be manufactured from well-established PDMS fabrication process. To provide Flow Channel bi-directional flow and aspiration flow as well as injection solution, multiple syringe pumps will be utilized, thus the entire flow circuit will be controlled by LabView to reduce human effort involved.

6. Conclusion

In this dissertation, we present a new device for massively-parallelized ultrahigh throughput cellular manipulation via mechanoporation. This new device is an interim instrumentation for UHT active microinjection device, which provides utility in and of itself.

The device concept and design is shown, with detailed feature size consideration and corresponding operation feasibility estimation. In terms of microfluid-providing aspiration pressure, cell transfer, capture, penetration and release can be realized by a single piece of instrumentation. The millimeter scale device chip containing ten thousand hemispherical capture wells monolithically integrating with Solid Penetrators is devised to perform thousands of cells manipulation within minutes. Sizes of capture well and Solid Penetrators are determined based on test cells we used in the validation studies (K562 cells and MEF cells). Manipulation operating parameters, such as cell membrane penetration force and corresponding aspiration pressure, cell speed, flow rate, etc. are analytically analyzed and numerically simulated, which agree with other research studies in the related application, and exhibit reasonable operation feasibility without detrimental effect on cells. Those estimated operating parameters also provide basis to develop test models in practical cell studies.

The device fabrication utilized conventional silicon MEMS technologies, and we successfully produced device chip with ten thousand roughly hemispherical capture wells, monolithically integrating with less than $0.5\mu\text{m}$ - tip size Solid Penetrators. A single chip

fabrication usually can be completed within a month, and batch fabrication experiment is underway to expedite manufacture.

A flow circuit system involving a syringe pump, pressure transducer, fixture set supporting the device chip was developed. Preliminary device functional test was carried out, and demonstrated robustness of the chip functional core membrane. Pressure drop with different flow rates was also characterized, which conforms to prediction. Device validation tests using K562 cells obtained about 15% average penetration efficiency of live cells after manipulation. Subsequent fluorescent beads and MEF cell tests identified several key issues resulting in this lower-than-expected efficiency, including bubble blocking and unoptimized manipulation parameters (capturing / puncturing flow rate and time). Observation of continuously increasing aspiration pressure during puncturing is another issue that could cause cell lysis and result in low penetration efficiency of live cells. Thus, improvement of cell manipulation results with system and operation optimization is possible.

The completed device is a development to address limitations of microinjection in biomedical and clinical applications, which not only achieves massive parallelization in mechanoporation, but also demonstrates a way for future accomplishment of the full-functional UHT active microinjection system as a primary study. Current outcomes verify the system concept that mechanoporation is a safe and efficient new means for cellular manipulation, and UHT cellular manipulation is possible, which will have potential to benefit numerous applications, e.g. molecular and cellular biology, genetic engineering, drug discovery, cell-based therapeutics.

References

- [1] K. Korn and E. Krausz, "Cell-based high-content screening of small-molecule libraries", *Current Opinion in Chemical Biology*, 2007, vol.11, pp.503-510.
- [2] M. Takehashi, M. Kanatsu-Shinohara, H. Miki, J. Lee, Y. Kazuki, K. Inoue, N. Ogonuki, S. Toyokuni, M. Oshimura, A. Ogura and T. Shinohara, "Production of knockout mice by gene targeting in multipotent germline stem cells", *Developmental Biology*, 2007, vol.312, pp.344-352.
- [3] I. R. Gilmore, S. P. Fox, A. J. Hollins and S. Akhtar, "Delivery Strategies for siRNA-mediated Gene silencing", *Current Drug Delivery*, 2006, vol.3, pp.147-155.
- [4] D. de Semir, M. Nadal, J. R. Gonzalez, S. Larriba, A. Avinyo, V. Nunes, T. Casals, X. Estivill and J. M. Aran, "Suitability of oligonucleotide-mediated cystic fibrosis gene repair in airway epithelial cells", *Journal of Gene Medicine*, 2003, vol.5, pp.625-639.
- [5] M. Boukallel, M. Gauthier, E. Piat, J. Abadie and C. Roux, "Microrobots for in vitro fertilization applications", *Cellular and Molecular Biology*, 2004, vol.50, pp.267-274.
- [6] S. Karkare and D. Bhatnagar, "Promising nucleic acid analogs and mimics: characteristic features and applications of PNA, LNA, and morpholino", *Applied Microbiology and Biotechnology*, 2006, vol.71, pp.575-586.
- [7] C. Mueller and T. R. Flotte, "Gene Therapy for Cystic Fibrosis", *Clinical Reviews in Allergy & Immunology*, 2008, vol.35, pp.164-178.
- [8] C. A. Fernandez and K. G. Rice, "Engineered Nanoscaled Polyplex Gene Delivery Systems", *Molecular Pharmaceutics*, 2009, vol.6, pp.1277-1289.

- [9] J. Lisziewicz, D. I. Gabrilovich, G. Varga, J. Q. Xu, P. D. Greenberg, S. K. Arya, M. Bosch, J. P. Behr and F. Lori, "Induction of potent human immunodeficiency virus type 1-specific T-cell-restricted immunity by genetically modified dendritic cells", *Journal of Virology*, 2001, vol.75, pp.7621-7628.
- [10] B. Demeneix, Z. Hassani and J. P. Behr, "Towards multifunctional synthetic vectors", *Current Gene Therapy*, 2004, vol.4, pp.445-455.
- [11] S. Mehier-Humbert and R. H. Guy, "Physical methods for gene transfer: Improving the kinetics of gene delivery into cells", *Advanced Drug Delivery Reviews*, 2005, vol.57, pp.733-753.
- [12] A. Noori, P. R. Selvaganapathy and J. Wilson, "Microinjection in a microfluidic format using flexible and compliant channels and electroosmotic dosage control", *Lab on a Chip*, 2009, vol.9, pp.3202-3211.
- [13] N. S. Yang, J. Burkholder, B. Roberts, B. Martinell and D. McCabe, "Invivo and Invitro Gene-Transfer to Mammalian Somatic-Cells by Particle Bombardment", *Proceedings of the National Academy of Sciences of the United States of America*, 1990, vol.87, pp.9568-9572.
- [14] K. E. Steele, K. Stabler and L. VanderZanden, "Cutaneous DNA vaccination against Ebola virus by particle bombardment: Histopathology and alteration of CD3-positive dendritic epidermal cells", *Veterinary Pathology*, 2001, vol.38, pp.203-215.
- [15] J. Gehl, "Electroporation: theory and methods, perspectives for drug delivery, gene therapy and research", *Acta Physiologica Scandinavica*, 2003, vol.177, pp.437-447.

- [16] M. Joergensen, B. Agerholm-Larsen, P. E. Nielsen and J. Gehl, "Efficiency of Cellular Delivery of Antisense Peptide Nucleic Acid by Electroporation Depends on Charge and Electroporation Geometry", *Oligonucleotides*, 2011, vol.21, pp.29-37.
- [17] P. F. Lurquin, "Gene transfer by electroporation", *Molecular Biotechnology*, 1997, vol.7, pp.5-35.
- [18] S. Mitragotri, "Innovation - Healing sound: the use of ultrasound in drug delivery and other therapeutic applications", *Nature Reviews Drug Discovery*, 2005, vol.4, pp.255-260.
- [19] T. Leighton, "The acoustic bubble", 1997, Academic Press.
- [20] J. Sundaram, B. R. Mellein and S. Mitragotri, "An experimental and theoretical analysis of ultrasound-induced permeabilization of cell membranes", *Biophysical Journal*, 2003, vol.84, pp.3087-3101.
- [21] W. Tao, J. Wilkinson, E. J. Stanbridge and M. W. Berns, "Direct Gene-Transfer into Human Cultured-Cells Facilitated by Laser Micropuncture of the Cell-Membrane", *Proceedings of the National Academy of Sciences of the United States of America*, 1987, vol.84, pp.4180-4184.
- [22] F. Scherer, M. Anton, U. Schillinger, J. Henkel, C. Bergemann, A. Kruger, B. Gansbacher and C. Plank, "Magnetofection: enhancing and targeting gene delivery by magnetic force in vitro and in vivo", *Gene Therapy*, 2002, vol.9, pp.102-109.
- [23] F. Krotz, H. Y. Sohn, T. Gloe, C. Plank and U. Pohl, "Magnetofection potentiates gene delivery to cultured endothelial cells", *Journal of Vascular Research*, 2003, vol.40, pp.425-434.

- [24] X. F. Cui, D. Dean, Z. M. Ruggeri and T. Boland, "Cell Damage Evaluation of Thermal Inkjet Printed Chinese Hamster Ovary Cells", *Biotechnology and Bioengineering*, 2010, vol.106, pp.963-969.
- [25] A. Adamo and K. F. Jensen, "Microfluidic based single cell microinjection", *Lab on a Chip*, 2008, vol.8, pp.1258-1261.
- [26] S. Sakai, S. Youoku, Y. Suto, M. Ando and A. Ito, "Automated high-throughput microinjection system for floating cell", *Proc. of SPIE*, 2005, vol.5699, pp.59-66.
- [27] D. V. McAllister, M. G. Allen and M. R. Prausnitz, "Microfabricated microneedles for gene and drug delivery", *Annual Review of Biomedical Engineering*, 2000, vol.2, pp.289-313.
- [28] R. W. Bernstein, M. Scott and O. Solgaard, "BioMEMS for high-throughput handling and microinjection of embryos", *Proc. of SPIE*, 2004, vol.5641, pp.67-73.
- [29] T. Shibata, S. Yamanaka, N. Kato, T. Kawashima, M. Nomura, T. Mineta and E. Makino, "Fabrication of micromanipulator array for cell patterning", *Microelectronic Engineering*, 2009, vol.86, pp.1439-1442.
- [30] E. Cornell, W. W. Fisher, R. Nordmeyer, D. Yegian, M. Dong, M. D. Biggin, S. E. Celniker and J. Jin, "Automating fruit fly *Drosophila* embryo injection for high throughput transgenic studies", *Review of Scientific Instruments*, 2008, vol.79, pp.1-7.
- [31] W. H. Wang, X. Y. Liu, D. Gelinas, B. Ciruna and Y. Sun, "A Fully Automated Robotic System for Microinjection of Zebrafish Embryos", *Plos One*, 2007, vol.2, pp.1-7.

- [32] K. Chun, G. Hashiguchi, H. Toshiyoshi and H. Fujita, "Fabrication of array of hollow microcapillaries used for injection of genetic materials into animal/plant cells", *Japanese Journal of Applied Physics Part 2-Letters*, 1999, vol.38, pp.L279-L281.
- [33] G. Cabodevila, B. Lepioufle and H. Fujita, "Arrayed Micro Needles for Mechanical Gene Insertion", *Proc. of SPIE*, 2002, vol.4937, pp.90-97.
- [34] S. Park, Y. S. Kim, W. B. Kim and S. Jon, "Carbon Nanosyringe Array as a Platform for Intracellular Delivery", *Nano Letters*, 2009, vol.9, pp.1325-1329.
- [35] D. B. Peckys, A. V. Melechko, M. L. Simpson and T. E. McKnight, "Immobilization and release strategies for DNA delivery using carbon nanofiber arrays and self-assembled monolayers", *Nanotechnology*, 2009, vol.20, pp.1-8.
- [36] A. V. Melechko, V. I. Merkulov, T. E. McKnight, M. A. Guillorn, K. L. Klein, D. H. Lowndes and M. L. Simpson, "Vertically aligned carbon nanofibers and related structures: Controlled synthesis and directed assembly", *Journal of Applied Physics*, 2005, vol.97, pp.1-39.
- [37] I. Obataya, C. Nakamura, S. Han, N. Nakamura and J. Miyake, "Nanoscale operation of a living cell using an atomic force microscope with a nanoneedle", *Nano Letters*, 2005, vol.5, pp.27-30.
- [38] X. J. Zhang, S. Zappe, R. W. Bernstein, O. Sahin, C. C. Chen, M. Fish, M. P. Scott and O. Solgaard, "Micromachined silicon force sensor based on diffractive optical encoders for characterization of microinjection", *Sensors and Actuators a-Physical*, 2004, vol.114, pp.197-203.

- [39] Y. Sun, K. T. Wan, K. P. Roberts, J. C. Bischof and B. J. Nelson, "Mechanical property characterization of mouse zona pellucida", *Ieee Transactions on Nanobioscience*, 2003, vol.2, pp.279-286.
- [40] J. L. V. Broers, E. A. G. Peeters, H. J. H. Kuijpers, J. Endert, C. V. C. Bouten, C. W. J. Oomens, F. P. T. Baaijens and F. C. S. Ramaekers, "Decreased mechanical stiffness in LMNA-/- cells is caused by defective nucleo-cytoskeletal integrity: implications for the development of laminopathies", *Human Molecular Genetics*, 2004, vol.13, pp.2567-2580.
- [41] Y. H. Tan, D. Sun, W. H. Huang and S. H. Cheng, "Mechanical Modeling of Biological Cells in Microinjection", *Ieee Transactions on Nanobioscience*, 2008, vol.7, pp.257-266.
- [42] M. Chizari and B. Wang, "Estimating Material Property and Failure of a Living Cell; Numerical Study", *International Journal of Applied Mechanics*, 2009, vol.1, pp.339-347.
- [43] Z. Lu, P. C. Y. Chen, H. Luo, J. Nam, R. W. Ge and W. Lin, "Models of maximum stress and strain of zebrafish embryos under indentation", *Journal of Biomechanics*, 2009, vol.42, pp.620-625.
- [44] Y. H. Tan, D. Sun, W. H. Huang and S. H. Cheng, "Characterizing Mechanical Properties of Biological Cells by Microinjection", *Ieee Transactions on Nanobioscience*, 2010, vol.9, pp.171-180.
- [45] S. Suresh, "Biomechanics and biophysics of cancer cells", *Acta Biomaterialia*, 2007, vol.3, pp.413-438.
- [46] C. Pozrikidis, "Fluid dynamics: theory, computation, and numerical simulation", 2001, Kluwer Academic Publishers.

- [47] J. Seo, C. Ionescu-Zanetti, J. Diamond, R. Lal and L. P. Lee, "Integrated multiple patch-clamp array chip via lateral cell trapping junctions", *Applied Physics Letters*, 2004, vol.84, pp.1973-1975.
- [48] C. J. M. van Rijin and M. C. Elwenspoek, "Micro filtration Membrane Sieve with Silicon Micro Machining for Industrial and Biomedical Applications", *Proc. IEEE*, 1995, pp.83-87.
- [49] R. Zazpe, C. Hibert, J. O'Brien, Y. H. Lanyon and D. W. M. Arrigan, "Ion-transfer voltammetry at silicon membrane-based arrays of micro-liquid-liquid interfaces", *Lab on a Chip*, 2007, vol.7, pp.1732-1737.
- [50] U. B. T. Giang, D. Lee, M. R. King and L. A. DeLouise, "Microfabrication of cavities in polydimethylsiloxane using DRIE silicon molds", *Lab on a Chip*, 2007, vol.7, pp.1660-1662.